Climate
of the Past

Discussions

EGU

Cretaceous Oceanic Anoxic Events prolonged by phosphorus cycle feedbacks

Sebastian Beil[1], Wolfgang Kuhnt[1], Ann Holbourn[1], Florian Scholz[2], Julian Oxmann[2], Klaus Wallmann[2], Janne Lorenzen[3], Mohamed Aquit[4], El Hassane Chellai[5]

[1]Institute of Geosciences, Christian-Albrechts-University, Ludewig-Meyn-Str. 10-14, D-24118 Kiel, Germany
[2]Geomar Helmholtz Centre for Ocean Research Kiel, Wischhofstr. 1-3, D-24148 Kiel, Germany
[3]Janne Lorenzen, Christian-Albrechts-University, Ludewig-Meyn-Str. 10-14, D-24118 Kiel, Germany
[4]OCP S.A., Direction de Recherche et Développement, Recherche Géologique, 46300 Youssoufia, Morocco
[5]Department of Geology, Faculty of Sciences Semlalia, Cadi Ayyad University, Marrakech, Morocco

Correspondence to: Sebastian Beil (Sebastian.Beil@ifg.uni-kiel.de) or Wolfgang Kuhnt (Wolfgang.Kuhnt@ifg.uni-kiel.de)

Abstract. Oceanic Anoxic Events (OAEs) document major perturbations of the global carbon cycle with repercussions on the Earth's climate and ocean circulation that are relevant to understand future climate trends. Here, we compare sedimentation patterns, nutrient cycling, organic carbon accumulation and carbon isotope variability across Cretaceous Oceanic Anoxic Events OAE1a and OAE2 in two drill cores with unusually high sedimentation rates from the Vocontian Basin (southern France) and Tarfaya Basin (southern Morocco). OAE1a and OAE2 exhibit remarkable similarities in the evolution of their $\delta^{13}C$ excursion with long-lasting negative carbon isotope excursions preceding the onset of both anoxic events, supporting the view that OAEs were triggered by massive emissions of volcanic CO_2 into the atmosphere. Based on analysis of cyclic sediment variations, we estimated the duration of the individual phases within the carbon isotope excursions. For both events, we identify: (1) a precursor phase lasting ~430 kyr and ~130 kyr, (2) an onset phase of ~390 and ~70 kyr, (3) a peak phase of ~600 and ~90 kyr, (4) a plateau phase of ~1400 and ~200 kyr and (5) a recovery phase of ~630 and ~440 kyr, respectively. The total duration of the positive carbon isotope excursion is estimated as 3400 kyr and 790 kyr and that of the main carbon accumulation phase as 980 kyr and 180 kyr, for OAE1a and OAE 2 respectively. The extended duration of the peak, plateau and recovery phases requires fundamental changes in global nutrient cycles either (1) through excess nutrient inputs to the oceans by increasing continental weathering and river discharge or (2) through nutrient-recycling from the marine sediment reservoir. We investigated the role of phosphorus on the development of carbon accumulation by analysing phosphorus speciation across OAE2 and the mid-Cenomanian Event (MCE) in the Tarfaya Basin. The ratios of organic carbon and total nitrogen to reactive phosphorus (C_{org}/P_{react} and N_{total}/P_{react}) prior to OAE2 and the MCE hover close to or below the Redfield ratio characteristic of marine organic matter. Decreases in reactive phosphorus resulting in C_{org}/P_{react} and N_{total}/P_{react} above the Redfield ratio during the later phase of OAE2 and the MCE indicate leakage from the sedimentary column into the water column under the influence of intensified and expanded oxygen minimum zones. These results suggest that a positive feedback loop, rooted in the benthic phosphorus cycle, contributed to increased marine productivity and carbon burial over an extended period of time during OAEs.

1 Introduction

The Cretaceous period was characterized by high atmospheric CO_2-levels and temperatures and episodic deposition of sediments with extremely high organic carbon content, referred to as Oceanic Anoxic Events (OAEs; e.g., Schlanger and Jenkyns, 1976; Jenkyns, 1980). These events represent prolonged and intense perturbations of the global carbon cycle (e.g., Arthur et al., 1985) associated with widespread anoxia in most ocean basins. Oceanic Anoxic Events are also characterized by positive carbon isotope ($\delta^{13}C$) excursions that have been related to globally enhanced rates of organic carbon burial (e.g., Berger and Vincent, 1986; Kump, 1991). The most prominent of these events were OAE1a during the early Aptian and OAE2 at the Cenomanian/Turonian boundary. Smaller events of probably more regional extent were also identified in several ocean basins (e.g., OAE 1b, c, d and OAE3). The triggering mechanisms and internal processes that are essential for sustaining high primary productivity over extended periods of time remain enigmatic. One of the limitations for understanding the driving mechanisms and dynamics of OAEs is the uncertainty about the duration of OAEs and individual phases within these events. Previous estimates differed substantially (Table 1), partly due to differing definitions of the onset and end of OAEs, based on the extent of organic-rich sediment accumulation or of the carbon isotope excursion. For instance, the positive $\delta^{13}C$ shift in the initial part of the excursion is considered to represent the entire OAE1a (e.g., Li et al, 2008, Moullade et al., 2015), whereas the return to background values (e.g., Sageman et al., 2006) or the end of the $\delta^{13}C$ plateau (e.g., Eldrett et al., 2015) are included into the definition of OAE2.

Carbon isotope excursions associated with OAEs are commonly characterized by an initial negative excursion, which has been attributed to the rapid release of a large volume of ^{13}C-depleted carbon either as methane and CO_2 from organic material in terrigenous soils and sediments, dissociation of submarine methane hydrates, or direct volcanic exhalation of CO_2 and thermal combustion of organic-rich sediments driven by volcanic heat flux (e.g., Dickens et al., 1995; Jenkyns, 2003; Erba, 2004; Turgeon and Cesar, 2008; Du Vivier et al., 2014). The following major positive carbon isotope excursion is generally attributed to largely enhanced burial rates of ^{12}C enriched organic carbon in marine organic-rich shales and/or in terrestrial peat and coal deposits (e.g., Jenkyns, 1980; Schlanger et al., 1987; Arthur et al., 1988). Key constraints on the subsequent feedback mechanisms of nutrient and carbon cycles are the rates at which the carbon was released and buried. Fast release rates would be consistent with catastrophic events, such as methane hydrate dissociation or thermal combustion of organic-rich sediments, whereas slower rates would implicate other processes. Burial rates influence the balance between continuing release of ^{13}C-depleted carbon and the relative impact of sequestration through enhanced biological productivity and globally intensified and expanded ocean anoxia.

Different hypotheses have been put forward to explain the enhanced accumulation of organic matter in Cretaceous sediments (e.g., Arthur et al., 1988; Jenkyns, 2010) and the processes triggering and maintaining global anoxia and enhanced primary productivity during OAEs. These include fertilization by nutrient input in the ocean system in association with the activity of large igneous provinces (LIPs) (e.g., Schlanger et al., 1981; Larson, 1991; Trabucho-Alexandre et al., 2010), sea level controlled remobilization of nutrients from flooded low altitude land areas associated with major marine transgressions (e.g.,

Mort et al., 2007, 2008), or release of phosphorus as a main limiting nutrient from sediments into the water column under anoxic bottom water conditions (Ingall and Jahnke, 1994; Slomp and Van Cappellen, 2007). However, the extent and the conditions under which phosphorus was available to act as a fertilizer for marine productivity during Cretaceous OAEs as well as the mechanisms and internal feedbacks that sustained OAEs for several hundred thousand years remain controversial.

70   Primary production in the modern marine environment is mainly limited by the availability of nitrogen, iron and phosphorus with the latter considered the ultimate limiting nutrient on longer geological timescales (Holland, 1978; Broecker and Peng, 1982; Codispoti, 1989; Smith, 1984; Tyrell, 1999; Filipelli, 2008). It has been suggested that the phosphorus budget of the modern ocean is imbalanced, since input fluxes from riverine, aeolian and ice-rafted sources do not fully match phosphorus burial in marine sediments and the hydrothermal removal of dissolved phosphate from the deep ocean (e.g., Wallmann,

75   2010). The main sink of phosphorus in the modern ocean are hemipelagic and shelf sediments, where the exposure to well-oxygenated water masses leads to almost complete remineralisation of organic matter and precipitation of authigenic phosphorus minerals (Ruttenberg, 1993). Phosphorus remains bound to manganese- and iron-oxides and -hydroxides in deep-sea sediments underlying well-oxygenated bottom water masses, which typically exhibit C:P below the Redfield ratio. Excess phosphate is released from shelf and continental margin sediments deposited in low oxygen environments, resulting

80   in elevated sedimentary C:P ratios. Today, estimates of residence time vary between 10 and 17 kyr (Ruttenberg, 2003) and 80 kyr (Broecker and Peng, 1982), depending on variable estimates of burial rates within the different marine phosphorus sinks, in particular in shallow seas and along continental margins (Ruttenberg, 2003). During Cretaceous OAEs, the extent and burial efficiency of these sinks must have varied in a fundamental way, due to sea-level and redox oscillations that affected marginal seas (e.g., Danzelle et al., 2018).

85   The main source for phosphorus in the oceans is terrigenous discharge of rivers in the form of dissolved inorganic phosphorus (DIP) and organic phosphorus (DOP), particulate inorganic phosphorus (PIP) and particulate organic phosphorus (POP). The delivery rate of POP and immediately bioavailable, reactive DIP and DOP to the ocean is strongly controlled by continental weathering and seasonal riverine discharge (Ruttenberg, 2003; Li et al., 2017a) and may, thus, have strong links to the variability of atmospheric carbon dioxide concentrations and the hydrological cycle during OAEs. Most sedimentary

90   rocks and sea floor sediments are characterized by low concentrations of phosphorus <0.13 % (Riggs, 1979) and shallow marine environments are considered as the main phosphorus sinks (Ruttenberg, 1993). In these sediments, a variety of phosphorus species are discriminated (Supplementary Material S1).

There are conflicting views on the influence of expanding OMZs or ocean anoxia on the phosphorus cycle and, in particular, whether sediments in OMZs serve as a phosphorus source or sink. It has been argued that oxygen depleted bottom waters

95   favour phosphorus release from the sediment to the water column (Ingall and Jahnke, 1994) and could stimulate primary production in surface waters (Wallmann, 2003). This in turn would result in increased organic carbon export flux, leading to higher oxygen demand, expansion and intensification of oxygen minima and a positive feedback with benthic phosphorus release (Slomp and Van Cappellen, 2007; Wallmann, 2010). In contrast, other studies suggested that intensified phosphorus burial occurs under anoxic conditions in shallow water environments, based on observations of calcium fluorapatite (CFA)

Climate
of the Past
Discussions

100   precipitation in present-day shallow water oxygen-depleted upwelling areas (Schulz and Schulz, 2005; Arning et al., 2009a,
       b; Goldhammer et al., 2010; Ingall, 2010; Cosmidis et al., 2013). On a long-term scale, the formation of CFA is
       approximately in balance with enhanced phosphorus release from anoxic sediments, implying that the dissolved oceanic
       phosphorus inventory is largely unaffected by regional changes in oxygen concentrations (Delaney, 1998; Anderson et al.,
       2001; Roth et al., 2014). However, this equilibrium may be disturbed during periods with expanded and intensified OMZs

105   and deep-water anoxia, as in the Mediterranean Sea during sapropel formation (Slomp et al., 2004) and in the Cretaceous
       ocean during OAEs (e.g., Mort et al., 2007, 2008).

       Observations and model simulations indicated that global warming enhances the terrestrial input of biologically reactive
       phosphorus to the marine environment, leading to increased production and burial of organic carbon in marine sediments
       (Mackenzie et al., 2002). Greenhouse gas forcing on ocean oxygenation, organic carbon burial and the phosphorus cycle is a

110   critical issue for understanding the onset, development and recovery of the ocean system from OAEs. In this study, we focus
       on two of the largest events, OAE1a and OAE2, with unusually expanded sediment records in two different ocean basins
       (Fig. 1). Time series analyses of high-resolution proxy records are used to determine the duration of individual phases within
       these carbon isotope excursions. In addition, we analyse phosphorus speciation across the mid-Cenomanian carbon isotope
       event (MCE) and OAE2 to investigate relationships to changing sea level, OMZ intensity and carbon burial and to test the

115   hypothesis of redox controlled phosphorus release as a nutrient source initiating and/or enhancing carbon burial during
       OAEs.

2 Material and Methods

2.1 Sediment cores

       Core SN°4 (27°59'46.4'' N, 12°32'40.6'' W) was retrieved in the Tarfaya Basin (southern Morocco), 40 km east of the town

120   Tarfaya, close to the road to Tan Tan. The marine sediment succession in the 350 m long Core SN°4, which provides an
       expanded record of OAE2, was deposited in an outer shelf setting within a subsiding basin on a passive margin during the
       Late Cretaceous. Late Albian to Turonian sedimentary stable isotope and geochemical records were previously presented by
       Beil et al. (2018) and Scholz et al. (2019). High-resolution XRF-scanner, bulk sediment stable isotope and carbon records
       across the onset of OAE2 were provided by Kuhnt et al. (2017). Here, we complement these records with phosphorus

125   speciation data and time-series analysis of logging natural gamma ray and high resolution XRF-scanner elemental
       distribution data across OAE2.

       Cores LB1 (43°14'37'' N, 5°34'12'' E; 70 m long) and LB3 (43°14'42'' N, 5°34'52'' E; 56 m long) were drilled near
       Roquefort-La Bédoule, 16 km southeast of Marseille in southern France. During the Aptian, the coring sites were located
       within an isolated intrashelf basin, the South Provence Basin, on the North Provençal carbonate Platform, where an

130   expanded succession of marine sediments including OAE1a accumulated. Details of the drilling operation were published by
       Flögel et al. (2010), detailed lithologic descriptions of the cores, biostratigraphy and intermediate resolution carbonate and

4

Climate
of the Past
Discussions

stable isotope measurements by Lorenzen et al. (2013) and Moullade et al. (2015). Here we present new high-resolution bulk carbonate isotope data across the precursor, onset and peak phases of OAE1a as well as time-series analysis of logging natural gamma ray and XRF-scanner elemental distribution data from a spliced composite record of LB1 and LB3. The tie point between both cores is at a depth of 49.4 m (Section 34, 3 cm section depth) in LB3 and 10.83 m (Section 8, 95 cm section depth) in LB1, below bed 170, identified by Moullade et al. (2015) as a prominent correlating feature. The tie point was set at the base of a prominent, extended maximum in XRF-core-scanning derived Log(Terr/Ca) (Section 2.3), present in both cores.

2.2 NGR-Logging

Wireline borehole logging of the SN°4 drill hole was carried out by Geoatlas (Laayoune, Morocco) using a Century geophysical logging system with natural gamma ray (NGR) sensor. For borehole logging of the LB1 and LB3 drill holes, an Antares Aladdin logging system with GR5 sensor probe was deployed. All logging operations were conducted shortly after completion of the drilling operation in boreholes without metal casing. Natural Gamma Ray (NGR) data are presented as American Petroleum Institute radioactivity units in counts per second (cps) with vertical resolutions of 0.1 m for SN°4, 0.05 m for LB1 and 0.025 m for LB3. More detailed information for SN°4 is given in Beil et al. (2018) and for LB1 and LB3 in Flögel et al. (2010), Lorenzen et al. (2013) and Moullade et al. (2015).

2.3 XRF-core-scanning and linescan imaging

Detailed descriptions of XRF-scanning of Core SN°4 are provided in Kuhnt et al. (2017) and Beil et al. (2018). Sections were scanned with a second generation Avaatech X-ray fluorescence scanner at the Christian-Albrechts-University, Kiel. Surfaces were covered with a 4 µm thick Ultralene foil after cleaning with fine-grained sandpaper. Data for this study are from the 10 kV dataset scanned with a spatial resolution of 1 cm (vertical slit of 1 cm, horizontal slit of 1.2 cm) measured with 10 kV, 750 µA, no filter and 10 s acquisition time. Sections of Cores LB1 and LB3 were polished with fine-grained sandpaper and covered with 4 µm thick Ultralene foil. The XRF-data from the 10 kV dataset presented in this study were measured with a spatial resolution of 1 cm with the tube setting of 10 kV, 250 µA and no filter with 15 s acquisition time.

Raw XRF-spectra of all three cores were converted with the iterative least-square package *Win Axil batch* (Canberra Eurisys) and the 10 kV Kiel model into element specific area counts. The Jai CV-L 107 3 CCD color linescan camera installed in the Avaatech XRF-scanner at the Christian-Albrechts-University (Kiel) was used to obtain core images with a downcore resolution of 143 ppcm for Cores SN°4, LB1 and LB3. We used the logarithmic ratios of elemental counts to eliminate XRF-core-scanning-specific effects like matrix-effect, grain size effect or variations in rock density (Weltje and Tjallingii, 2008). Log(Terr/Ca) is used as a proxy for terrigenous, clastic material vs. marine biogenic carbonate. Elements of typically terrigenous origin (Terr) detected with the 10 kV settings of the Avaatech 2. Generation XRF scanner are aluminium (Al), iron (Fe), potassium (K), silicon (Si) and titanium (Ti) (e.g., Peterson et al., 2000; Calvert and Pedersen, 2007; Mulitza et al., 2008; Tisserand et al., 2009; Govin et al., 2012). In contrast, calcium (Ca) is assumed to be of marine origin, mainly

consisting of shells and tests of organisms. Log(K/Al) is widely used to analyse the composition of clay assemblage

165   (Weaver, 1967, 1989; Niebuhr, 2005). We assume that the ratio is primarily controlled by variations in the amount of

potassium-rich illite in the clay mineral assemblage and therefore reflects weathering intensity in the source area (Calvert

and Pedersen, 2007).

2.4 Stable Isotopes

Organic and bulk carbonate stable isotope data from Core SN°4 were compiled from the high-resolution record of the onset

170   of OAE2 (Kuhnt et al., 2017) and from the lower resolution record over the entire core (Beil et al., 2018). Bulk carbonate

samples were analysed with the Finnigan MAT 251 and MAT 253 mass spectrometers at the Leibniz Laboratory for

Radiometric Dating and Stable Isotope Research at the Christian-Albrechts-University (Kiel). The accuracy for carbon

isotopes was ±0.05 ‰ and ±0.08 ‰ for oxygen isotopes. Organic carbon stable isotopes were analysed at the GeoZentrum

Nordbayern (Erlangen) with a Flash EA 2000 elemental analyzer coupled to a Thermo Finnigan Delta V Plus mass

175   spectrometer on samples with a spacing between ~0.1 and ~2.3 m. Measurement accuracy was ±0.06 ‰. Results are reported

on the delta scale as $\delta^{18}O$, $\delta^{13}C_{carbonate}$ and $\delta^{13}C_{org}$ against the Vienna PeeDee belemnite standard (VPDB).

Initial lower resolution stable isotope data from Cores LB1 and LB3 were presented in Lorenzen et al. (2013) and Moullade

et al. (2015). Published data have a depth resolution of ~20 cm in LB1 and ~40 cm in LB3. Additional samples were

analysed to increase the resolution to ~5 cm during the early part of OAE1a between 18 and 41.5 m in Core LB1. Stable

180   isotopes of bulk carbonate samples were analysed at the Leibniz Laboratory for Radiometric Dating and Stable Isotope

Research at the Christian-Albrechts-University (Kiel) with a Finnigan MAT 251 mass spectrometer. Analytical uncertainty

for stable carbon isotopes was ±0.04 ‰ and ±0.07 ‰ for stable oxygen isotopes. Results are reported on the delta scale as

$\delta^{18}O$ and $\delta^{13}C_{carbonate}$ against the Vienna PeeDee belemnite standard (VPDB).

2.5 Phosphorus speciation and analysis of major and trace elements

185   The distribution of major and trace elements and phosphorus speciation were determined on new samples from Core SN°4,

mainly taken close to the published organic stable isotope samples (Beil et al., 2018). Samples cover the interval between

42.11 m (Section 18, Segment 3, 23-24 cm) and 305.77 m (Section 111, Segment 2, 29-31 cm). The core was sampled every

~2.4 m with increased resolution of ~1.2 m over the global isotope excursions OAE2 and MCE. The surface of samples was

cleaned with a metal free porcelain knife and ground down with a rotary mill with agate balls to prevent metallic

190   contaminations. The powdered material was subdivided into aliquots for major and trace elements analysis and material for

determination of phosphorus speciation. A further aliquot was used for carbonate and organic carbon measurements for

samples not close to the already published organic isotope samples. Additional samples from high carbonate content

intervals were prepared and measured to determine the influence of low clay and organic content.

2.5.1 Analysis of major and trace elements

195 Aliquots of 100 mg were weighed into PTFE vessels. Each sample was treated with 2 cm^3 HF, 2 cm^3 HNO$_3$ and 3 cm^3 HClO$_4$, sealed and heated for 8 hours at 185 °C. The acid was subsequently smoked off at 190 °C. The almost dry residue was dissolved again in 1 cm^3 HNO$_3$, smoked off and dissolved again in 5 cm^3 ultrapure water and 1 cm^3 HNO$_3$ to be heated again for 2 hours in sealed vessels. The solution was finally transferred and diluted with 10 ml HNO$_3$ in volumetric flasks. The solutions were measured with a VARIAN 720-ES ICP-OES for major elements and an Agilent Technologies 7500
200 Series ICP-MS for trace elements at GEOMAR Helmholtz Centre for Ocean Research Kiel.

2.5.2 Phosphorus speciation

Samples for the measurement of phosphorus speciation were aliquots from samples used for the analysis of major and trace elements. A modified CONVEX extraction method (Oxmann et al., 2008; Fig. S2) was used to extract Ca-bound and Al/Fe-oxyhydroxide bound phosphorus. The sample material (250 mg) was subsequently three times treated with 3.75 ml
205 KCl/EtOH, decanted and supernatants discarded. Al/Fe-bound phosphorus was extracted from the centrifuged residue with the addition of first 3.75 ml NaOH/Na$_2$SO$_4$ (incubated for 1 h at 25 °C), then 3.75 ml NaOH/Na$_2$SO$_4$ (incubated for 2h at 99 °C) and finally 7 ml Na$_2$SO$_4$. Solutions were centrifuged and decanted after each of the three treatment steps and stored for measurement. The centrifuged residue was decarbonated for 8h with 3.75 ml H$_2$SO$_4$. The Ca-bound phosphorus fraction was extracted by adding further 3.75 ml H$_2$SO$_4$ (incubated for 2h at 99 °C) and twice Na$_2$SO$_4$ (3.75 and 7 ml). Each of the three
210 steps was followed by centrifugation and decanting of the solution. Supernatants of each step were again mixed and stored for measurements. Details are provided in Fig. S2.

For measurement of Ca-bound phosphorus, an aliquot of 0.1 ml was diluted with 4.9 ml MilliQ. Concentrations of Fe-/Al-bound phosphorus were measured on 4.5 ml of sample solution equilibrated with the addition of 0.5 ml of sol7 (Table S3) to pH of ~1. Concentrations of Al/Fe- and Ca-bound phosphorus were calibrated with the PO$_4$-Merck Standard (1000 mg
215 PO$_4$/l) diluted to specific concentrations. The ammonium molybdate solution (0.1 ml; Supplementary Material S4) was added 30 min before measurements. For samples close to the photometric saturation level a new aliquot was diluted to lower concentration within the measurement range. A detailed list with used chemicals and respective concentrations is available as Table S3.

2.6 Total organic carbon, carbonate and nitrogen content

220 Aliquots of samples for determination of major and trace elements and phosphorus speciation in Core SN°4 were analysed for total organic carbon (TOC), carbonate and nitrogen content. Replicates of 8 – 10 mg sample material were pulverized, homogenized and sealed into tin capsules for the determination of Total Carbon (TC) and Nitrogen (N) and into silver capsules followed by decarbonatization with 0.25 N hydrochlorid acid (HCl) to measure TOC. Different weights of Acetanilid (10.36 % N, 71.09 % C) and of the certified soil standard BSTD1 (0.216 % N, 3.5 % C) were sealed and

225   measured for calibration and for monitoring of long-term stability. All capsules were measured with a Carlo Erba
        Proteinanalyzer NA1500 at the Geomar Helmholtz Centre for Ocean Research, Kiel. Carbonate content (TIC) was calculated
        as TIC = (TC – TOC) * 8.3333.

2.7 Time series analysis

        The package *astrochron* (Meyers and Sageman, 2007; Meyers et al., 2012a; Meyers, 2014) for R (R Core Team, 2017) was
230   used to perform frequency analysis on the NGR and XRF (Log(Terr/Ca)) datasets. The NGR-datasets were linearly
        interpolated to a spatial resolution of 0.1 m for Core SN°4 and 0.025 m for the spliced dataset of Cores LB3 and LB1. XRF-
        derived Log(Terr/Ca) from LB3/LB1 was linearly interpolated to a spatial resolution of 0.01 m. Long-term variability of >20
        m wavelengths was removed from the NGR dataset by using a Gaussian kernel smoother with the function *noKernel* of
        astrochron.

235   Dominant frequencies in Cores LB3 and LB1 were extracted with an implementation of the robust red noise MTM analysis
        of Mann and Lees (1996) using the function *mtmML96* (Patterson et al., 2014) of *astrochron* with five 2π prolate tapers.
        Visualization and checks were performed with the *eha*-function of *astrochron* with three 2π prolate tapers and a window of 6
        m over the frequency range between 0 and 4 cycles/m for the spliced record of LB3 and LB1. Identical intervals and
        frequency ranges were used to check results with the complementary XRF-derived dataset Log(Terr/Ca) for LB3LB1 (Fig.
240   S5).

        Ages for Core SN°4 are derived by correlating the NGR record to that of the neighbouring Core S13 (Meyers et al., 2012a)
        following Kuhnt et al. (2017). A total of 14 tiepoints delimiting characteristic features of both cores were used. The age
        model of Meyers et al. (2012a) was transferred into chronological ages by anchoring the Cenomanian/Turonian boundary at
        the top of cycle 3 to the chronological age of 93.9 Ma (Meyers et al., 2012b).

245   Periodicities for precession, obliquity and eccentricity are based on the orbital solution La04 (Laskar et al., 2004). Additional
        periodicities for eccentricity were extracted from the orbital solutions La10a-d (Laskar et al., 2011a) for the Cenomanian and
        Aptian intervals and La10a-d and La11 (Laskar et al. 2011a, b) for the Cenomanian interval using the *astrochron*-function
        mtmML96 (Patterson et al., 2014). The analysis of orbital parameters for OAE1a was limited to the Aptian interval (Fig. S6)
        between 113 and 126 Ma and to the Cenomanian interval between 93 and 99 Ma for OAE2. Ratios were calculated for the
250   main frequencies. Periodicities and ratios of the different orbital cycles are presented in Table S7 for the Aptian and in Table
        S8 for the Cenomanian interval.

2.8 Phosphorus and organic carbon accumulation rates in Core SN°4

        Bulk sediment mass accumulation rates (MAR) were calculated by multiplication of linear sedimentation rates (LSR;
        derived from the age model of Core SN°4) with an average dry bulk density (DBD) of 2.1 g cm^{-3}. Mean density for the
255   interval encompassing OAE2 (600 - 2000 kyr) in neighbouring Core S13 (Meyers et al., 2012a) is 2.08 g cm^{-3} (StDev 0.12 g
        cm^{-3}). Phosphorus accumulation rates (PAR) were calculated by multiplying MAR with phosphorus concentrations from

discrete measurements. Organic carbon accumulation rates (TOCAR) were calculated using the organic carbon concentrations from Kuhnt et al. (2017) and Beil et al. (2018).

3 Results

3.1 Bulk carbonate and organic carbon δ¹³C across OAE1a and OAE2

We identified five common phases (precursor, onset, peak, plateau and recovery) in the $\delta^{13}C$-records of OAE1a and OAE2 (Fig. 2, 3 and Supplementary Material S9). The interval preceding both OAEs is characterized by constant long-term means without discernible trends and low variability. A precursor phase of two to four distinct $\delta^{13}C$ minima (negative excursions) precedes the onset of the positive carbon isotope excursion. The onset phase encompasses the entire interval of increasing $\delta^{13}C$ towards the first prominent peak. The peak phase is defined as the interval from maximal values of the first peak until the end of the second peak. A characteristic plateau phase (interval of nearly constant $\delta^{13}C$ values) follows the second peak of the carbon isotope excursions. A recovery phase comprises the return of $\delta^{13}C$-values to background levels after the OAE excursions.

The decrease between the preceding background level and the minimum within the second trough is comparable in amplitude with 0.7 ‰ for OAE1a and 0.4 ‰ for OAE2. The most positive values of the $\delta^{13}C$ isotope excursion are reached at the first peak of OAE2 at 103.22 m with -24.2 ‰. In contrast, values continue to increase during OAE1a with highest values of 4.9 ‰ during the plateau stage at 40.11 m. The difference between the last minimum of the precursor phase and the first maximum of the peak phase is 2.4 ‰ for OAE1a and 4.6 ‰ for OAE2. Considering the differing trend of OAE1a, with further increases during the plateau stage, the total amplitude of OAE1a is 3.6 ‰. Differences of mean values between the background levels before and after the OAE are 0.3 ‰ for OAE2 (from -28.5 ‰ (StDev 0.3 ‰) before to -28.2 ‰ (StDev 0.2 ‰) after OAE2) and 0.8 ‰ for OAE1a (from 1.9 ‰ (StDev 0.1 ‰) before to 2.7 ‰ (StDev 0.2 ‰) after OAE1a) indicating a general increase in background $\delta^{13}C$ after the OAEs.

3.2 Bulk carbonate δ¹⁸O across OAE1a and OAE2

The $\delta^{18}O$ datasets share common trends, despite a possible lithological influence in the upper part of the sedimentary record of OAE1a in LB3. Transient cooling events, identified by transient $\delta^{18}O$ increases in LB3/LB1 and SN°4, occur during the early phases of both OAEs (Fig. 2, 3 and S11). A detailed description of the Plenus Cold Event (Gale and Christensen, 1996; Jarvis et al., 2011; Jenkyns et al., 2017) during OAE2, also associated with prominent foraminiferal extinctions, was presented in Kuhnt et al. (2017). The 3-stepped cooling during OAE2 started already during the onset of the positive carbon isotope excursion or onset phase. The main cooling event occurred within the trough between the peaks during the peak phase. The stable oxygen isotope record of OAE1a shows a similar response of global temperatures to excess organic carbon burial. The main increase in $\delta^{18}O$ precedes the end of the onset phase. A second minor increase follows transient warming

Climate
of the Past
Discussions

during the peak phase. Similarities in the $\delta^{18}O$ records of both events imply a comparable response of global temperatures to lowered atmospheric pCO_2-levels caused by excess carbon drawdown due to the burial of vast amount of organic material on a global scale.

290   **3.3 Regional differences in terrigenous input during OAE2 and OAE1a**

The different paleogeographic settings and depositional environments of Cores SN°4, LB1 and LB3 result in important differences in the regional terrigenous sediment input. The XRF-derived Log(Terr/Ca) (Fig. 2) in the Tarfaya Basin exhibits low variability throughout with lowest values during OAE2. In contrast, Log(Terr/Ca) (Fig. 3) shows higher amplitude variability during OAE1a. A major increase in Log(Terr/Ca) from -1.69 to -0.87 during the onset of OAE1a between 68.09

295   and 67.99 m indicates either a decrease in carbonate deposition or an increase in terrigenous input. Following this increase, the NGR and Log(Terr/Ca) records exhibit high amplitude and high frequency variability during C4 to C6 (26 - 23.29 m) and during the latter part of C7 and C8 (49.7 – 0 m) (Fig. 3, 4 and S5).

3.4 Characteristic orbital periodicities over OAE1a and OAE2

Periodicities for precession, obliquity and eccentricity from the orbital solutions La04 (Laskar et al., 2004) and La10a-d

300   (Laskar et al., 2011a) were calculated by power spectral analysis for the Aptian (113 and 126 Ma, Fig. S6 and Table S7) and Cenomanian (93 to 99 Ma, Table S8 and Beil et al., 2018) intervals. The analysis of the Aptian interval reveals highly significant periodicities (>99 % Confidence level, CL) of 403.76 kyr (long eccentricity e1), 124.29 kyr (short eccentricity e2) and 95.04 kyr (short eccentricity e3) and minor peaks at 131.59 kyr (short eccentricity; e2) and 99.25 kyr (short eccentricity; e3). Highly significant (CL > 99 %) obliquity periodicities are 46.97 (o1) and 36.98 kyr (o2). Major precessional

305   periodicities are 22.27 (p1) and 18.03 (p2) kyr. Major periodicities in the Cenomanian interval are 405.49 kyr (long eccentricity e1), 127.14 kyr (short eccentricity e2) and 96.79 kyr (short eccentricity e3). Three highly significant periodicities for obliquity are detected with the strongest peak at 37.64 kyr (o2). Weaker periodicities are 48.24 kyr (o1) and 28.07 kyr (o3). A weaker but still highly significant (CL >99 %) peak is detected at 1.3 Myr which could reflect the long modulation of obliquity. The strongest precessional peaks are 22.46 kyr (p1), 21.36 kyr (p2) and 18.33 kyr (p3).

310   **3.5 Duration and subdivisions of OAE1a**

The spliced NGR-record of LB3 and LB1 across OAE1a was subdivided into 5 intervals of relatively consistent orbital periodicities (N1 to N5), based on EHA-analysis of the cyclic patterns (Fig. 4, S12 and S13). The recognition of cyclic patterns in the NGR record during OAE1a allowed correlation of major frequencies with orbital periodicities of Laskar et al. (2004, 2011a, 2011b) and calculation of mean sedimentation rates. The correlation is based on the comparison of the ratios

315   of different extracted orbital periodicities from the NGR-record (Fig. 4 and S13) with those from the orbital solutions of Laskar et al. (2004, 2011a, 2011b) (Fig. S6 and Table S7). Identified frequencies and their orbital interpretation for different depth intervals are presented in Table S14 together with resulting mean sedimentation rates. Table 2 shows the comparison

with durations of Malinverno et al. (2010) for the different C-stages of Menegatti et al. (1998). A stronger response of the depositional system to variations in obliquity and precession in the latest part of stage C2 precedes the onset of OAE1a (Fig. 4, S5 and S13). Another period of strong response to orbital obliquity forcing in the NGR- and Log(Terr/Ca) time series (Fig. 4 and S5) occurs during later stages of OAE1a, starting during the middle or later part of stage C7 and persisting after the end of OAE1a. The same trend to high short-term variability is also recorded in core images, $\delta^{13}C_{carbonate}$ and $\delta^{18}O$ and related to pronounced lithological changes between carbonate-rich and clay-rich beds (Fig. 3).

Sedimentation rates (Table S14) increase from C3 and C4 with 1.37 cm kyr^{-1} to the recovery phase C8 with 3.07 cm kyr^{-1}. An overall stable ratio between terrigenous and carbonate content, as indicated by Log(Terr/Ca) (Fig. 3), suggests a continuous increase in both carbonate and terrigenous input.

3.6 Duration and subdivisions of OAE2

The NGR-record of Core SN°4 (Fig. S15) for the interval encompassing OAE2 (140 and 23 m) was correlated to the orbitally-tuned record of Core S13 (Meyers et al., 2012a). Sedimentation rates before the onset of OAE2 are 8.2 cm kyr^{-1}. A drop to 4.1 cm kyr^{-1} occurs during the positive carbon isotope excursion. Following a second interval of lower sedimentation rates (4.3 cm kyr^{-1}) in the upper part of the plateau phase, sedimentation rates recover to ~8 cm kyr^{-1}, which is comparable to levels preceding OAE2.

EHA-analysis (Fig. 5) reveals a strong response of the sedimentary system to obliquity (mainly o1, 48 kyr) and short eccentricity (e2/e3, 100 kyr) forcing during the OAE2 carbon isotope excursion. Based on this response, OAE2 (positive carbon isotope excursion) in Core SN°4 lasted for 790 kyr including and 360 kyr without the recovery phase. Response to orbital forcing is particularly strong during the peak phase (~90 kyr), which encompasses a pronounced short eccentricity cycle and parts of the recovery phase (~440 kyr), while the plateau phase (~200 kyr) is characterized by a dampened response to orbital forcing.

Four $\delta^{13}C_{org}$ minima (precursor phase) precede the positive $\delta^{13}C$ excursion of OAE2 over a time interval of ~130 kyr. The onset phase of OAE2 (~70 kyr), defined as the interval between the centre of the last $\delta^{13}C_{org}$ minimum and the first $\delta^{13}C_{org}$ maximum of OAE2, is subdivided into three phases. The initial steep increase lasts 31 kyr, the intermediate plateau 14 kyr and the final rise to the first peak of the carbon isotope excursion 24 kyr. The time interval between the two maxima in $\delta^{13}C_{org}$ (peak phase) is ~90 kyr. The duration of the plateau phase defined as the period between the second maximum and the end of the plateau in $\delta^{13}C_{org}$ is ~200 kyr. The recovery phase between the end of the plateau and the return to background values after OAE2 had a duration of 440 kyr.

3.7 Temporal evolution of OAE1a and OAE2

The precursor phase of OAE1a (C3 of Menegatti et al., 1998) consists of an extended interval of low $\delta^{13}C_{carbonate}$ (<1.75 ‰), encompassing two prominent minima (<1.5 ‰). It immediately precedes the positive $\delta^{13}C$ excursion and lasts for 434 kyr.

The precursor phase of OAE2 is characterized by 4 nearly equally spaced minima (<28.5‰) in $\delta^{13}C_{org}$ lasting ~126 kyr. The
last two prominent minima immediately precede the onset of OAE2 and last for 75 kyr. The onset phase of the positive
isotope excursion has a duration of 388 kyr for OAE1a (C4 of Menegatti et al., 1998) and 68 kyr for OAE2. The peak phase
lasts 596 kyr in OAE1a (C5 and C6) and 86 kyr in OAE2, the plateau phase extends over 1398 kyr in OAE1a (C7) and 204
in OAE2 and the final recovery phase has a duration of 625 kyr for OAE1a (C8) and 435 kyr for OAE2. The precursor, onset
and peak phases are consistently ~5 times longer in OAE1a than in OAE2, while the plateau phase is more than ~7 times
longer. The recovery phase is almost of the same duration, taking into account uncertainties in defining the change point at
the end of each excursion.

3.8 Sedimentary phosphorus

Total phosphorus (P_{total}) concentrations in Core SN°4 (Fig. 6) are overall below 5 mg g^{-1} except during two periods of
enrichment peaking at 220.19 m with 16.61 mg g^{-1} and at 104.4 m with 7.53 mg g^{-1}. Corresponding peaks in P_{total}/Al give a
weight ratio of 1.07 at 220.19 m and 1.20 at 104.4 m. Concentrations and variability of P_{total} are low in the lowermost (305 –
267 m) and uppermost (67.51 – 42.11 m) parts of the studied interval with means of 0.54 mg g^{-1} (StDev 0.19 mg g^{-1}) and
0.86 mg g^{-1} (StDev 0.3 mg g^{-1}), respectively. The attribution of phosphorus to initial sources within the sediments is difficult
as the different fraction extracted by the CONVEX method are operationally defined. Earlier studies found finely distributed
fish debris and fecal pellets in Cenomanian sediments of the Tarfaya basin (e.g., El Albani et al., 1999), partially
reprecipitated as phosphate nodules during early diagenesis (e.g., Leine, 1986; Kuhnt et al., 1997). The dissolution of
phosphorus fixed in iron-aluminum crusts and the degradation of organic matter followed by reprecipitation as calcium
bound phosphorus further complicate the reconstruction of the initial source of phosphorus.

3.9 Phosphorus speciation

Concentrations of reactive Phosphorus (P_{react}; Fig. 7) in Core SN°4 calculated by summing up Al/Fe- and Ca-bound
phosphorus are on average ~89 % of total phosphorus (P_{total}; Fig. 6) measured with ICP-OES. Organic-matter-bound
phosphorus was not considered due to methodological limitations (Golteman, 2001) and remineralization and reprecipitation
(sink-switching) into more stable Al/Fe- and Ca-bound phosphorus species during early diagenesis. Differences are caused
by not extractable phosphorus bound in insoluble minerals or adhesively bound phosphorus extracted and discarded during
the first step with KCl/EtOH (Fig. S2).
Concentrations of phosphorus bound to aluminum- or iron-oxyhydroxides (AlFeP; Fig. 7) are low (median 0.014 mg g^{-1}).
Increased concentrations (mean 0.027 mg g^{-1}) are determined for the lowermost interval between 305 and 272.58 m,
followed by an interval with lower average concentration (mean 0.014 mg g^{-1}) and lower variability (StDev 0.006 mg g^{-1})
until 72.09 m. The uppermost interval is again characterized by increased variability (StDev 0.008 mg g^{-1}). Calcium-bound
phosphorus (CaP; Fig. 6) is the dominant species in the studied interval of Core SN°4. Concentrations are below 4 mg g^{-1}

380   except for two periods of enrichment peaking at 220.19 and 104.4 m with 15.76 and 6.62 mg g^{-1}, respectively. Both maxima coincide with maximum enrichment of total phosphorus.

The overall low and nearly constant concentrations of Al/Fe-bound phosphorus in Core SN°4 (Fig. 6) imply either constant anoxic or euxinic conditions causing desorption of phosphorus bound to aluminum- and iron-oxyhydroxides during deposition or early diagenesis or early diagenetic conversion of Al/Fe-bound phosphorus into authigenic phosphorus-

385   carbonates. The onset of episodic dysoxic to anoxic conditions occurs during the early Cenomanian (above 273 m) in Core SN°4 and consistently oxygen depleted to anoxic environmental conditions prevail after the termination of the MCE above 185 m, based on the XRF-core scanner derived ratio Log(Mn/S) (Beil et al., 2018). Increased concentrations of Al/Fe-bound phosphorus and a decreased AlFeP/P_{total} ratio (Fig. 6 and 7) below 270 m support a better oxygenated depositional environment and are therefore in line with these observations. However, low variability in Al/Fe-bound phosphorus and

390   AlFeP/P_{total} ratio between 270 and 185 m, albeit in an interval of low sampling resolution, do not support the episodic spread of anoxia in the transition interval between 273 and 185 m (Beil et al., 2018). Concentrations of Ca-bound phosphorus (Fig. 6) decrease slightly with the onset of OAE2 above 103.34 m. These lower concentrations of Al/Fe-bound phosphorus and a stable ratio of Ca- to Al/Fe-bound phosphorus rather suggest a secondary, syn- or post-depositional conversion of Al/Fe-bound phosphorus into Ca-bound phosphorus.

395   The ratio of Ca- to Al/Fe-bound phosphorus (CaP/AlFeP; Fig. 6) shows three prominent maxima peaking at 220.19, 143.51 and 104.4 m. The lowermost (305 – 228.68 m) and uppermost (102.16 – 42.11 m) intervals show a decreased variability of 37.5 and 19.5. All these characteristics are reflected in the sum of Ca- and Al/Fe-bound phosphorus except for the peak at 143.51 m that is caused in case of the CaP/AlFeP-ratio by a drop in Ca-bound phosphorus.

The atomic ratio of organic carbon to $P_{reactive}$ (defined as the sum of loosely sorbed, organic, authigenic and iron bound

400   phosphorus) was interpreted by Anderson et al. (2001) as a proxy for marine paleoproductivity. Due to sink switching (transfer to different phosphorus pools) between the different phosphorus species especially during early diagenesis the authors assumed that most phosphorus in the different pools is originally derived from the remineralization of organic material and could therefore be seen equivalent to P_{org}. Here, P_{react} is calculated by summing up the two CONVEX-derived P-pools CaP (seen as equivalent to P_{auth}) and AlFeP. Both loosely absorbed and organic P were not measured. It is assumed

405   that the concept of Andersen et al. (2001) is applicable, as both extracted P-pools (CaP and AlFeP) contain the majority of P_{total} (mean = 89 %; Fig. S16).

The atomic ratios of C_{org} and N_{total} against P_{react} were calculated (Fig. 7). Both ratios show very similar trends except for the lower part between 305.77 and 258.35 m that is characterized in N_{total}/P_{react} by increased values (median 5.9) and in C_{org}/P_{react} by low values and low variability (median 77.6, StDev 34.9), albeit in an interval with low resolution. Afterwards both ratios

410   show similar characteristics of low values (median of C_{org}/P_{react} 89.1 and of N_{total}/P_{react} 3.5) and low variability (StDev of C_{org}/P_{react} 67.1 and of N_{total}/P_{react} 1.9) until 104.4 m punctuated by short-lived maxima during the MCE (average of C_{org}/P_{react} 170 and of N_{total}/P_{react} 7.5). OAE2 is again characterized by markedly increased ratios (maxima of C_{org}/P_{react} 1123.8 and of N_{total}/P_{react} 29.6). The uppermost part is characterized by increased values (median of C_{org}/P_{react} 242.6 and of N_{total}/P_{react} 7.3).

The ratio of CONVEX-extracted AlFeP to P_{total} (Fig. 7) shows increased values (mean 0.058) in the lower part between 305
415   and 272.58 m followed low ratios (mean 0.014) until the top of the sampled interval of Core SN°4.

3.10 Temporal changes in P-species concentrations and accumulation rates

Two maxima in P_{total} in the Cenomanian interval of Core SN°4 coincide with maxima in P_{total}/Al (Fig. 6). The more
prominent of these phosphorus enrichments (peaking at 220.19 m) precedes the onset of the MCE by ~3.04 m. The second
maximum at 104.4 m occurs during the onset phase of OAE2 and coincides with a transient $\delta^{13}C$ minimum, approximately
420   halfway in the increase towards the first $\delta^{13}C_{org}$ maximum at 103.22 m (Fig. 6 and S11).

The ratio of Ca-bound to Al/Fe-bound phosphorus (Fig. 6) is characterized by three prominent peaks at 220.19, 143.51 and
104.40 m. Two of these peaks at 220.19 and 104.40 m are also characterized by high P_{total} concentrations and maxima in the
P_{total}/Al ratio. The first peak at 220.19 m precedes the first increase in $\delta^{13}C_{org}$ of the MCE, and the second peak at 104.4 m
occurs within the onset phase of the $\delta^{13}C_{org}$ excursion of OAE2. Both peaks of CaP/AlFeP and P_{total} coincide with minima in
425   the C_{org}/P_{total}-ratio (Fig. S16), suggesting an inorganic source of the deposited phosphorus or enhanced recycling of organic
carbon and reprecipitation of the organic-bound phosphorus as Ca-bound phosphorus.

The increase in the atomic C_{org}/P_{total}-ratio (Fig. S17) during OAE2 postdates the increase in the atomic C_{org}/N_{total}-ratio,
interpreted by Beil et al. (2018) as enhanced cycling of nitrogen rich organic matter within a dysoxic or anoxic water
column. The increase in C_{org}/P_{total} starts immediately above the prominent peak in Ca-/AlFe-bound and total phosphorus and
430   coincides with the first $\delta^{13}C_{org}$ maximum of OAE2 (Fig. 6). The highest C_{org}/P_{total} ratio is determined at 90.78 m within the
plateau phase of OAE2. This peak coincides with minima in P_{total} and P_{total}/Al implying remobilization either synsedimentary
due to preferential recycling of phosphorus in the water column and/or at the sediment. This decrease in P_{total}-content is
paralleled by a decrease in C_{org} (Fig. 6), suggesting enhanced remobilization of phosphorus as well as organic matter.

The atomic ratios of C_{org}/P_{react} and N_{total}/P_{react} are shown in Fig. 7 and compared to the respective Redfield ratio (Redfield,
435   1958; Redfield et al., 1963) representative of the mean composition of marine phytoplankton assumed to represent the main
source of organic matter and sedimentary phosphorus to the sediments. Both ratios are always lower or close to the Redfield
ratio (C:N:P of 106:16:1), except for two intervals. The first falls within the MCE when C_{org}/P_{react} is equal to or higher than
106:1 and N_{total}/P_{react} is close to the predicted ratio of 16:1. The second interval starts during OAE2 above the prominent peak
in P_{total}, synchronous with the Transgressive Surface (TS) of Ce5. Both ratios surpass predicted values at the first maximum
440   in $\delta^{13}C_{org}$, decrease slightly during the interval influenced by the Plenus Cold Event and show a large increase during the
Plateau Phase. The remaining part of the sampled interval is characterized by increased values above the background level
that is characteristic for the lower part of Core SN°4 until the onset of OAE2.

Three different intervals across OAE2 are characterized by different phosphorus accumulation rates of specifically P_{react}, but
also P_{total}, Al/Fe-bound P and Ca-bound P (Fig. 8). The first interval between 2100 and 1730 kyr (134.6 – 106.4 m) shows
445   increased accumulation rates of P_{react} (mean 0.0185 g cm^{-2} kyr^{-1}) interrupted by a prominent peak with a maximum of 0.064 g

cm^{-2} kyr^{-1} between 2010 and 1940 kyr (127.2 – 121.5 m) during the interval preceding OAE2 and the precursor and earliest onset phases. The second interval between 1730 and 1370 kyr (106.4 – 87.1 m) shows lower averages of 0.0059 g cm^{-2} kyr^{-1} between the early onset und plateau phase, interrupted by a prominent peak at 1799 kyr (110.8 m) with 0.0844 g cm^{-2} kyr^{-1} during the onset phase. The third interval between 1370 and 780 kyr (87.1 – 41.8 m) shows again increased accumulation

450   rates of on average 0.0143 g cm^{-2} kyr^{-1} during the recovery phase and after OAE2.

4 Discussion

4.1 Influence of paleogeographic setting and weathering regime

Changes in the weathering regime of the source area, as shown by the XRF-scanner derived Log(K/Al), influence the sedimentary record across OAE1a at La Bédoule (Fig. 3). Increased Log(K/Al) and higher δ^{18}O suggest predominantly

455   physical weathering and/or intensified erosion, characteristic for drier conditions, and/or markedly seasonal rainfall prior to OAE1a (C2 and early C3) at La Bédoule (Fig. 3 and 4). A decrease in Log(K/Al), synchronous with a shift to carbonate-depleted sediments, indicated by Log(Terr/Ca), coincides with an increase in δ^{18}O associated with the first transient cold event within the onset phase of OAE1a (C4). This covariance of δ^{18}O and Log(K/Al), in combination with published palynological and geochemical data (e.g., Masure et al., 1998; Hochuli et al., 1999; Keller et al., 2011; Föllmi, 2012; Cors et

460   al., 2015) suggest that the La Bédoule area was located at the northern edge of the subtropical high pressure desert belt and shifted into the northern hemisphere westerlies with increased rainfall during OAE1a. An equatorward contraction of the sub-tropical high-pressure belt also occurred in East Asia during the mid-Cretaceous warm period (Hasegawa et al., 2012). The paleo-location of La Bédoule (Cores LB3 and LB1) close to 30° N (Masse et al., 2000) would predispose the area for latitudinal changes of the Hadley cell with drier conditions in times of an expanded high-pressure belt and increased rainfall

465   resulting from an equatorward contracted Hadley cell. Strengthening fluctuations between drier and wetter climate conditions are recorded during the onset, main and early plateau phase. After a stabilization during the plateau phase, wet conditions prevail after the end of OAE1a.

The evolution of the weathering regime across OAE2 in the Tarfaya Basin differed substantially (Fig. 2), probably related to the lower paleolatitude and different paleoceanographic setting in a coastal upwelling area. The period before the onset of

470   OAE2 was characterized by low sea surface temperatures and high mean Log(K/Al) exhibiting high variability, suggesting orbital forcing of a monsoonal hydrological cycle and weathering regime. A shift to lower mean Log(K/Al), indicative of stronger chemical weathering and/or reduced monsoonal seasonality in the source area coinciding with low sea surface temperatures during the precursor phase suggests increased upwelling intensity and intensified monsoonal wind forcing. A shift back to higher Log(K/Al) indicating weaker chemical weathering in the source area occurred at the end of the plateau

475   phase of OAE2. The main interval of OAE2 (onset, peak and plateau phase) is characterized by intense chemical weathering and a weak response of the hydrological cycle to orbital forcing, suggesting that the hinterland of the Tarfaya Basin was

more or less permanently under the influence of tropical convective rainfall. The recovery phase and the immediate post-OAE2 period is again characterized by weaker chemical weathering and a stronger response to orbital forcing, typical for a monsoonal regime at the northern edge of the seasonal swing of the ITCZ. Persistently high temperatures (O'Brien et al.,

480   2017) in the recovery and post-OAE2 phase, as indicated by low $\delta^{18}O$ in SN°4, suggest that the equatorward shift of the monsoonal zone and southward expansion of the high-pressure desert belt occurred during a period of global warming. Changes in the weathering regime during the carbon isotope excursion may, thus, be linked to major fluctuations of atmospheric CO_2 levels associated with increased carbon burial and the strong response to local insolation forcing in the late onset and peak phase of OAE2 (Fig. 5).

4.2 Comparison of amplitude and duration of $\delta^{13}C$ excursions

4.2.1 Duration of OAEs

The estimated durations of OAEs vary substantially from minimum estimates of 45 kyr for OAE1b to >3 Myr for OAE1a, depending on the definition of individual OAEs (Table 1). Whereas there is a broader consensus to define the duration of OAE2 as the entire interval between the onset of the positive excursion and the end of the recovery phase, estimates for

490   OAE1a are usually restricted to the interval of organic rich sedimentation (Selli-Level). This interval encompasses the onset and peak of the $\delta^{13}C$ excursion but does not include the plateau and recovery phase (e.g., Malinverno et al., 2010). At La Bédoule, these differences result in durations of 1.1 Myr (onset and peak phases only) and of 3.1 Myr (including plateau and recovery phases), which corresponds to approximately four times the duration of OAE2.

Our estimated durations of OAE1a isotope stages agree with those of Malinverno et al. (2010) for the C6 to C8 stages (Table

495   2). Minor differences are caused by differing definitions of the boundaries between isotope stages in the Cismon core, in the higher resolution LB3/LB1 composite record and different calculations of orbital periods. The plateau phase (C7) lasts for 1260 kyr agreeing with the 1398 kyr of Malinverno et al. (2010) within the range of error. Sedimentation patterns at La Bédoule are predominantly controlled by orbital obliquity with varying influence of short eccentricity and periodic influence of precession. A marked increase in sedimentation rate occurred in the latest part of the plateau phase (C7), close to the

500   transition to the recovery phase (C8), which lasted for 630 kyr. Response to obliquity forcing in NGR and Log(Terr/Ca), as shown in EHA-analysis (Fig. 4 and S5) and power spectra (Fig. S13) intensified during the late plateau phase (C7) and dominated during the recovery phase (C8) and after the OAE1a isotope excursion.

Larger deviations from the estimates of Malinverno et al. (2010) are evident for isotope stages C5 and C4. Isotope stage C5 has a shorter duration of 280 kyr compared to 510 kyr, estimated in the Cismon core. In contrast, the main increase of the

505   positive carbon isotope excursion, corresponding to C4 (Menegatti et al., 1998), has a duration of 390 kyr in LB3/LB1, which is ~60 % longer than the estimate of 239 kyr by Malinverno et al. (2010). The duration of C4 is interpreted as a response to long eccentricity (405 kyr). Strong eccentricity control during the precursor phase (C3) and during the onset phase (C4) is supported by EHA-analysis and power spectra (Fig. 4 and S13), suggesting that orbital eccentricity influenced

the global carbon cycle and regional sedimentation. The largest differences are within the precursor phase (C3) with 440 kyr

510   in LB3/LB1 and 46.7 kyr in the Cismon core, which is probably caused by hiatuses in the Cismon APTICORE record. Malinverno et al. (2010) did not rule out the occurrence of smaller sedimentary gaps in the OAE1a sequence of the Cismon core, which are not long enough to compromise the complete biostratigraphic succession reconstructed by Erba et al. (1999).

4.2.2 Amplitude of carbon isotope excursions during OAE1a and OAE2

Carbon isotopes were measured on bulk carbonate for OAE1a at La Bédoule and on bulk organic matter in the Tarfaya

515   Basin, where organic matter is of marine origin and changes in $\delta^{13}C$ values, thus, mainly reflect global reservoir changes at intermediate values of local productivity (Van Bentum et al., 2012). The amplitude of carbon isotope excursions is generally larger for organic matter than for bulk carbonate (Jenkyns, 2010). This is also the case for OAE2 in the Tarfaya Basin, where a gradient of ~4 ‰ for organic $\delta^{13}C$ and ~2.5 ‰ for carbonate $\delta^{13}C$ was established in several cores across the basin (Kuhnt et al., 1986, 1990, 2005, 2017; Kolonic et al., 2005; Tsikos et al., 2004). However, large regional differences in the

520   amplitude of the $\delta^{13}C$ excursion in both organic and bulk inorganic carbon were also reported for OAE2 (Van Bentum et al., 2012; Wendler 2013; Kuhnt et al., 2017). Possible causes include local differences in the $\delta^{13}C$ of dissolved inorganic carbon dependent on local productivity, oxygenation and diagenesis (Kuypers et al., 1999; Jenkyns, 2010; Van Bentum et al., 2012; Kuhnt et al., 2017). Similar differences in the amplitude of the $\delta^{13}C$ excursion are recorded for OAE1a, where highest amplitudes reach or slightly exceed 4 ‰ in both organic carbon and carbonate (e.g., Menagatti et al., 1998), whereas at deep

525   water localities with distinct black shale deposition of the Selli event the amplitude remains lower (~2.5 ‰, Malinverno et al., 2010). Within the range of this high regional variability no systematic difference in the amplitude of the $\delta^{13}C$ excursion between OAE1a and OAE2 can be recognized, which is remarkable, since this would also imply a similar amount of organic carbon removed from the ocean/atmosphere into the sedimentary reservoir.

A long-term increase in $\delta^{13}C$ over the Cretaceous and early Cenozoic was reported by Katz et al. (2005) and attributed to the

530   evolution of large-celled phytoplankton and increased organic carbon burial efficiency in expanding depositional spaces (e.g., shallow shelves around the Atlantic), created during the rifting phase of the current Wilson cycle (Wilson, 1966; Worsley et al., 1986). Continuous removal of isotopically light organic carbon by deposition in shallow seas depleted the global carbon reservoir. The OAE1a and OAE2 records show differences in the background levels between the preceding intervals and after the terminations of both events with 0.8 ‰ in $\delta^{13}C_{carb}$ for OAE1a and 0.3 ‰ in $\delta^{13}C_{org}$ for OAE2. An

535   overall increase over OAE2 is also reconstructed for deposits of the English chalk (Jarvis et al., 2006). We assume that the long-term increase observed by Katz et al. (2005) was stepwise and to a large degree influenced by Cretaceous OAEs. The large-scale isotopic depletion of the global carbon reservoir accompanying these major disturbances of the global carbon cycle was not entirely compensated during the recovery phase and in the multimillion-year interval following these events inducing a long-term increase in $\delta^{13}C$ during the Cretaceous.

4.3 Impact of orbital forcing on the evolution of OAE1a and OAE2

The orbital configuration favouring enhanced marine biological productivity in low latitudes may have been different for OAE1a and OAE2. Recent studies (e.g., Batenburg et al., 2016; Kuhnt et al., 2017) tuned the onset of OAE2 to a 405 kyr eccentricity maximum that succeeded an extended period of low seasonality, caused by a 2.4 Myr eccentricity minimum, which would be associated with stronger obliquity forcing during the precursor phase. The much shorter onset phase of OAE2 suggests a faster and stronger response of the ocean system to the carbon cycle perturbation, either related to a shorter and more intense initial carbon dioxide release or to different orbital configuration such as higher amplitude eccentricity cycles. Additionally, higher rates of sea level rise would promote enhanced organic carbon burial in shallow shelf seas. These extensive dysoxic to anoxic shallow shelf seas would favour fast recycling of limiting nutrients, thereby enhancing primary production and further boosting organic carbon burial. Eccentricity control on both sea-level and organic carbon burial is also suggested by the ~90 and ~600 kyr durations of the peak phases of OAE2 and OAE1a (maximum organic carbon deposition and highest δ^{13}C values) (Fig. 4 and 5).

In contrast, a strong obliquity imprint is detected during the plateau phases (Fig. 4 and 5). A period of high amplitude obliquity forcing would steepen the latitudinal temperature gradient and intensify atmospheric circulation (Batenburg et al., 2016; Kuhnt et al, 2017), thus helping to maintain elevated biological productivity in the tropical oceans. However, recycling of essential nutrients from buried sediments or release from new sources (e.g., flood basalts of LIPs) would have been necessary to maintain this new equilibrium state over extended periods of time. The plateau stage lasted seven times longer during OAE1a than during OAE2, which excludes orbital forcing as a primary control on its duration. This is also suggested by differences in the response to orbital forcing at the end of the plateau phases which is characterized by a short episode of enhanced response to eccentricity forcing during OAE1a and persistent response to obliquity forcing during OAE2.

Orbital obliquity is the main pacemaker of climate oscillations during the recovery phase of both OAEs. Obliquity determines the summer intertropical insolation gradient which has recently been suggested as an important driver of changes in tropical and subtropical hydrology and sedimentation patterns (Bosmans et al., 2015). An increased insolation gradient between the tropical summer and winter hemisphere during high obliquity leads to intensified atmospheric circulation within the Hadley cell, resulting in stronger cross-equatorial winds and intensified moisture transfer into the summer hemisphere. Continental climate proxy data and models suggest a contraction of the Hadley cell and a latitudinal shift of the subtropical high-pressure belt towards the equator during mid-Cretaceous super-greenhouse conditions (Hasegawa et al., 2012; Hay and Flögel, 2012). This climate scenario would place the hinterland of the Tarfaya Basin in the dry hot subtropical desert climate zone during OAE2, whereas the La Bédoule area was likely influenced by the humid zone of the Northern Hemisphere westerlies during OAE1a. An increase of cross-equatorial winds and intensified rainfall at obliquity maxima would thus have affected the Tarfaya basin by increasing upper ocean mixing and upwelling and the La Bédoule area by increased rainfall due to intensified westerlies.

Periods of high amplitude 41 kyr obliquity variations last ~400-800 kyr and are separated by nodes of weak obliquity forcing with a duration of ~200-400 kyr (Fig. S6, Laskar et al., 2004). During the recovery phase of OAEs, obliquity-forced low latitude climate oscillations may have led to periods of enhanced equatorial upwelling, which would have promoted carbon

575   sequestration and, over several hundred thousand years, depleted the ocean's nutrient pool. A period of low 41 kyr variability in orbital obliquity (obliquity node), commonly associated with global cooling episodes in Cenozoic climate records (e.g., Pälike et al., 2006), ultimately terminated OAE1a and 2.

4.4 Role of phosphorus recycling in maintaining high productivity during OAEs

Phosphorus is the primary limiting nutrient controlling marine biological productivity on longer (i.e. geological) timescales

580   (e.g., Holland, 1978; Broecker and Peng, 1982; Codispoti, 1989; Smith, 1984). In contrast to nitrate, which can be synthesized from atmospheric nitrogen, the phosphorus supply to the ocean is restricted by riverine terrestrial input (Ruttenberg, 2003). This constitutes a limiting factor for increased marine primary productivity. Thus, alternative nutrient sources such as enhanced terrestrial input or recycling of marine sediments are necessary to sustain high primary productivity over extended periods of time typical for Cretaceous OAEs (e.g., Nedebragt et al., 2004).

585   C_{org}/P_{react} and N_{total}/P_{react} close to or above the Redfield ratio are measured within the MCE and OAE2 intervals, suggesting preservation of the initial atomic ratio of primary production, possibly even enhanced by a change in the phytoplankton community (Geider and La Roche, 2002) or depletion in P_{react}. Unusually high phosphorus values in the intervals preceding the MCE and during the onset of OAE2 are likely caused by starved sedimentation, which may be due to formation of hard grounds and condensed sections at sea-level high stands or winnowing of fine-grained sediment by intensified bottom

590   currents.

Regional changes in redox conditions towards anoxic or euxinic conditions in the lower water column would inhibit fixation of remobilized phosphorus in authigenic CaP, permitting the leakage of phosphorus into the water column, resulting in initial or increased sedimentary C:P and N:P ratios. Intensification of oxygen depletion during the plateau phase of OAE2 is associated with increasing C_{org}/P_{react} and N_{total}/P_{react} due to reduced diagenetic phosphorus precipitation permitting

595   phosphorus leakage from the sediment into the water column. Phosphorus accumulation rates, in contrast, start to decline earlier during the precursor phase of OAE2. A trend to more reducing conditions during the plateau and recovery phase of OAE2 was also suggested by Kolonic et al. (2005), based on high accumulation rates of redox-sensitive elements.

A similar sequence of events was reconstructed by Stein et al. (2011) for OAE1a in deposits from the Gorgo a Cerbara section (Umbria-Marche basin) in central Italy (Fig. S18). Phosphorus accumulation and C_{org}/P_{total} increased during the

600   precursor phase (C3 of Menegatti et al., 1998) and decreased during the onset phase (C4 of Menegatti et al., 1998), suggesting enhanced phosphorus recycling from the sediments, similar to the record of OAE2 in Core SN°4. Stein et al. (2011) also reported a minor increase of C_{org}/P_{total} at the base of the peak phase (C5+C6) and persistently high C_{org}/P_{total} during the late peak phase (C5+C6), in analogy to OAE2 in Core SN°4.

605 The impact of oxygen depletion on the release of phosphorus into the water column was shown by recent studies on modern Oxygen Minimum Zones (e.g., Noffke et al., 2012; Schollar-Lomnitz et al., 2019) with implications for increased primary productivity through feedback mechanisms. Phosphorus recycling from the sediments may have sustained high primary productivity over extended periods of time, thus, contributing to the long duration of OAE1a and OAE2. Phosphorus remobilization under anoxic conditions from vast areas of flooded shelf sediments facilitated high organic carbon burial rates during the onset, peak and plateau phases of the three anoxic events, and may have acted as a positive feedback process,

610 enhancing carbon burial and removal of light carbon isotopes from the marine dissolved inorganic carbon reservoir and resulting in positive carbon isotope excursions.

5 Conclusions

New high-resolution stable isotope and XRF-scanner data were integrated with published records from Cores LB3 and LB1 in the South Provence Basin (Lorenzen et al., 2013; Moullade et al., 2015) and from Core SN°4 in the Tarfaya Basin (Kuhnt

615 et al., 2017; Beil et al., 2018) to contrast the temporal evolution of two of the largest Oceanic Anoxic Events: OAE1a and OAE2. The structure of the marine $\delta^{13}C$ records suggests a similar evolution of the carbon cycle during both OAEs, although the duration of the individual phases differ substantially. Both OAEs exhibit negative excursions (precursor phase) with a duration of 430 kyr (OAE1a) and 130 kyr (OAE2), immediately preceding the onset of the positive carbon isotope excursion. The onset phases, lasting 390 kyr for OAE1a and 70 kyr for OAE2, are characterized by intervals of rapid $\delta^{13}C$ increase

620 separated by small plateaus with slower $\delta^{13}C$ change. Prominent cooling events recorded as $\delta^{18}O$ increases start during the latest onset phase and extend into the peak phase (Plenus Cold Event during OAE2), which last 600 kyr during OAE1a and only 90 kyr during OAE2. The plateau phase extends over 1400 kyr for OAE1a but lasts only 200 kyr for OAE2. However, the durations of the recovery phases are similar with 630 kyr (OAE1a) and 440 kyr (OAE2).

Phosphorus speciation data from Core SN°4 from the Tarfaya Basin covering the MCE and OAE2 were used to reconstruct

625 dynamics of this essential nutrient. Phosphorus speciation shows a predominance of Ca-bound phosphorus surpassing concentrations of Al/Fe-bound P by one to two orders of magnitude. Phosphorus bound to Al- and Fe-oxyhydroxides is elevated during the early Cenomanian (305 - 273 m) in Core SN°4, reflecting sedimentation in a shallower environment or less intensive redox-induced, early diagenetic cycling of iron oxyhydroxides, and during the early Turonian (74 - 42 m). Two of three increases in Ca-bound phosphorus / Al/Fe-bound phosphorus during the middle (222 – 218 m) and latest

630 Cenomanian (104 m), also characterized by increased P_{total} concentrations, are close to the Transgressive Surfaces of Ce2.1 and Ce5. Both enrichments are therefore interpreted as condensed horizons, caused by sediment starvation during sea level high stands.

Elevated ratios C_{org}/P_{react} and N_{total}/P_{react} during the global carbon isotope events MCE and OAE2 indicate a change in the water column towards more reducing conditions. Oxygen-free bottom water permitted the leakage of dissolved phosphorus

635 from the sedimentary column and increased the ratios of C_{org} and N_{total} to P_{react} within the sediments. This change is

20

apparently synchronous with enhanced organic carbon burial in the Tarfaya Basin. The delayed increase of C_{org}/P_{react} and N_{total}/P_{react} with respect to the $\delta^{13}C_{org}$ increase suggests that the Cenomanian OAEs were not initiated by shelfal phosphorus remobilization. However, the coincidence of maximum organic carbon burial and highest C_{org}/P_{react} and N_{total}/P_{react} underlines the significance of phosphorus leakage from sediments for maintaining high organic carbon burial rates necessary to sustain

640   globally recognized $\delta^{13}C$ shifts during OAEs over extended time periods.

Data availability

Newly acquired data from this study will be available at the Pangaea Data Repository.

Author contribution

Sebastian Beil, Wolfgang Kuhnt and Ann Holbourn designed the study and wrote the manuscript. Wolfgang Kuhnt, Ann

645   Holbourn, Sascha Flögel and Mohamed Aquit planned and supervised the drilling of Cores LB1, LB3 and SN°4. Data for this study were acquired by Sebastian Beil, Mohamed Aquit, Janne Lorenzen, Julian Oxmann, Florian Scholz, Klaus Wallmann, Ann Holbourn and Wolfgang Kuhnt. Time series analysis was performed by Sebastian Beil. El Hassane Chellai facilitated fieldwork and drilling. All authors read and provided comments on the manuscript.

Competing interests

650   The authors declare that they have no conflict of interest.

References

Anderson, L. D., Delaney, M. L., and Faul, K. L.: Carbon to phosphorus ratios in sediments: Implications for nutrient cycling. Global Biogeochem. Cy., 15(1), 65-79, https://doi.org/10.1029/2000GB001270, 2001.

Arning, E. T., Birgel, D., Brunner, B., and Peckmann, J.: Bacterial formation of phosphatic laminites off Peru. Geobiology, 7(3), 295-307, https://doi.org/10.1111/j.1472-4669.2009.00197.x, 2009a.

Arning, E. T., Lückge, A., Breuer, L. C., Gussone, N., Birgel, D., and Peckmann, J.: Genesis of phosphorite crusts off Peru. Mar. Geo., 262(1-4), 68-81, https://doi.org/10.1016/j.margeo.2009.03.006, 2009b.

Arthur, M. A., Dean, W. E. and Schlanger, S. O.: Variations in the Global Carbon Cycle During the Cretaceous Related to Climate, Volcanism, and Changes in Atmospheric CO$_2$, in: The Carbon Cycle and Atmospheric CO$_2$: Natural Variations Archean to Present, edited by: Sundquist, E., and Broecker, W., American Geophysical Union, Washington D.C., USA, 32, 504-529, https://doi.org/10.1029/GM032p0504, 1985.

Arthur, M. A., Dean, W. E., and Pratt, L. M.: Geochemical and climatic effects of increased marine organic carbon burial at the Cenomanian/Turonian boundary, Nature, 335, 714–717, https://doi.org/10.1038/335714a0, 1988.

Batenburg, S. J., De Vleeschouwer, D., Sprovieri, M., Hilgen, F. J., Gale, A. S., Singer, B. S., Koeberl, C., Coccioni, R., Claeys, P., and Montanari, A.: Orbital control on the timing of oceanic anoxia in the Late Cretaceous, Clim. Past, 12(10), 1995-2009, https://doi.org/10.5194/cp-12-1995-2016, 2016.

Beil, S., Kuhnt, W., Holbourn, A. E., Aquit, M., Flögel, S., Chellai, E. H., and Jabour, H.: New insights into Cenomanian paleoceanography and climate evolution from the Tarfaya Basin, southern Morocco, Cretaceous Res., 84, 451-473, https://doi.org/10.1016/j.cretres.2017.11.006, 2018.

Berger, W. H. and Vincent, E.: Deep-sea carbonates: reading the carbon-isotope signal, Geol. Rundsch., 75(1), 249-269, https://doi.org/10.1007/BF01770192, 1986.

Bornemann, A., Erbacher, J., Heldt, M., Kollaske, T., Wilmsen, M., Lübke, N., Huck, S., Vollmar, N. M., and Wonik, T.: The Albian–Cenomanian transition and Oceanic Anoxic Event 1d – an example from the boreal realm, Sedimentology, 64(1), 44-65, https://doi.org/10.1111/sed.12347, 2017.

Bosmans, J. H. C., Hilgen, F. J., Tuenter, E., and Lourens, L. J.: Obliquity forcing of low-latitude climate, Clim. Past, 11(10), 1335-1346, https://doi.org/10.5194/cp-11-1335-2015, 2015.

Broecker, W. S. and Peng, T.-H.: Tracers in the Sea. Eldigio Press, Palisades, New York, USA, 1982.

Calvert, S. E. and Pedersen, T. F.: Chapter fourteen elemental proxies for palaeoclimatic and palaeoceanographic variability in marine sediments: interpretation and application, in: Developments in Marine Geology, edited by: Hillaire–Marcel, C. and De Vernal, A., Elsevier, 1, 567-644, https://doi.org/10.1016/S1572-5480(07)01019-6, 2007.

Charbonnier, G., Boulila, S., Spangenberg, J. E., Adatte, T., Föllmi, K. B., and Laskar, J.: Obliquity pacing of the hydrological cycle during the Oceanic Anoxic Event 2, Earth Planet. Sc. Lett., 499, 266-277, https://doi.org/10.1016/j.epsl.2018.07.029, 2018.

Climate
of the Past
Discussions

Codispoti, L. A.: Phosphorus vs. nitrogen limitation of new and export production, in: Productivity of the Ocean: Present and Past, edited by: Berger, W. H., Smetacek, V. S., and Wefer, G., Wiley, New York, USA, 377–394, 1989.

695 Cors, J., Heimhofer, U., Adatte, T., Hochuli, P. A., Huck, S., and Bover-Arnal, T.: Climatic evolution across oceanic anoxic event 1a derived from terrestrial palynology and clay minerals (Maestrat Basin, Spain), Geol. Mag., 152(4), 632-647, https://doi.org/10.1017/S0016756814000557, 2015.

Cosmidis, J., Benzerara, K., Menguy, N., and Arning, E.: Microscopy evidence of bacterial microfossils in phosphorite crusts of the Peruvian shelf: Implications for phosphogenesis mechanisms, Chem. Geol., 359, 10-22, 700 https://doi.org/10.1016/j.chemgeo.2013.09.009, 2013.

Danzelle, J., Riquier, L., Baudin, F., Thomazo, C., and Pucéat, E.: Oscillating redox conditions in the Vocontian Basin (SE France) during Oceanic Anoxic Event 2 (OAE 2), Chem. Geol., 493, 136-152, https://doi.org/10.1016/j.chemgeo.2018.05.039, 2018.

Delaney, M. L.: Phosphorus accumulation in marine sediments and the oceanic phosphorus cycle. Global Biogeochem. Cy., 705 12(4), 563-572, http://dx.doi.org/10.1029/98GB02263, 1998.

Dickens, G. R., O'Neil, J. R., Rea, D. K., and Owen, R. M.: Dissociation of oceanic methane hydrate as a cause of the carbon isotope excursion at the end of the Paleocene, Paleoceanography, 10(6), 965-971, https://doi.org/10.1029/95PA02087, 1995.

Du Vivier, A. D., Selby, D., Sageman, B. B., Jarvis, I., Gröcke, D. R., and Voigt, S.: Marine ^{187}Os/^{188}Os isotope stratigraphy reveals the interaction of volcanism and ocean circulation during Oceanic Anoxic Event 2. Earth Planet. Sc. Lett., 389, 23-710 33, https://doi.org/10.1016/j.epsl.2013.12.024, 2014.

El Albani, A., Kuhnt, W., Luderer, F., Herbin, J. P., and Caron, M.: Palaeoenvironmental evolution of the Late Cretaceous sequence in the Tarfaya Basin (southwest of Morocco). Geol. Soc. (London) Spec. Publ., 153(1), 223-240, https://doi.org/10.1144/GSL.SP.1999.153.01.14, 1999.

Eldrett, J. S., Ma, C., Bergman, S. C., Lutz, B., Gregory, F. J., Dodsworth, P., Phipps, M., Hardas, P., Minisini, D., Ozkan, 715 A., Ramezani, J., Bowing, S. A., Kamo, S. L., Ferguson, K., Macaulay, C., and Kelly, A. E.: An astronomically calibrated stratigraphy of the Cenomanian, Turonian and earliest Coniacian from the Cretaceous Western Interior Seaway, USA: Implications for global chronostratigraphy, Cretaceous Res., 56, 316-344, https://doi.org/10.1016/j.cretres.2015.04.010, 2015.

Erba, E.: Calcareous nannofossils and Mesozoic oceanic anoxic events, Mar. Micropaleontol., 52(1-4), 85-106, 720 https://doi.org/10.1016/j.marmicro.2004.04.007, 2004.

Erba, E., Channell, J. E., Claps, M., Jones, C., Larson, R., Opdyke, B., Premoli Silva, I., Riva, A., Salvini, G., and Torricelli, S.: Integrated stratigraphy of the Cismon Apticore (southern Alps, Italy); a" reference section" for the Barremian-Aptian interval at low latitudes, J. Foramin. Res., 29(4), 371-391, 1999.

Erbacher, J., Huber, B. T., Norris, R. D., and Markey, M.: Increased thermohaline stratification as a possible cause for an 725 ocean anoxic event in the Cretaceous period, Nature, 409(6818), 325, https://doi.org/10.1038/35053041, 2001.

23

Filippelli, G. M.: The global phosphorus cycle: past, present, and future. Elements, 4(2), 89-95, https://doi.org/10.2113/GSELEMENTS.4.2.89, 2008.

Flögel, S., Kuhnt, W., and Moullade, M.: Drilling of Early Cretaceaous Oceanic Anoxic Event 1a in southern France, Scientific Drilling, 9, 20-22. https://doi.org/10.5194/sd-9-20-2010, 2010.

730 Föllmi, K. B.: Early Cretaceous life, climate and anoxia, Cretaceous Res., 35, 230-257, https://doi.org/10.1016/j.cretres.2011.12.005, 2012.

Föllmi, K. B., Bôle, M., Jammet, N., Froidevaux, P., Godet, A., Bodin, S., Adatte, T., Matera, V., Fleitmann, D., and Spangenberg, J. E.: Bridging the Faraoni and Selli oceanic anoxic events: late Hauterivian to early Aptian dysaerobic to anaerobic phases in the Tethys, Clim. Past, 8(1), 171-189, https://doi.org/10.5194/cp-8-171-2012, 2012.

735 Gale, A. S. and Christensen, W. K.: Occurrence of the belemnite Actinocamax plenus in the Cenomanian of SE France and its significance, Bull. Geol. Soc. Denmark, 43(1), 68-77, 1996.

Gambacorta, G., Malinverno, A., and Erba, E.: Orbital forcing of carbonate versus siliceous productivity in the late Albian– late Cenomanian (Umbria-Marche Basin, central Italy), Newsl. Stratigr., 52(2), 197-220, https://doi.org/10.1127/nos/2018/0456, 2019.

740 Geider, R. and La Roche, J.: Redfield revisited: variability of C:N:P in marine microalgae and its biochemical basis, Eur. J. Phycol., 37(1), 1-17, https://doi.org/10.1017/S0967026201003456, 2002.

Goldhammer, T., Brüchert, V., Ferdelman, T. G., and Zabel, M.: Microbial sequestration of phosphorus in anoxic upwelling sediments, Nat. Geosci., 3(8), 557, https://doi.org/10.1038/ngeo913, 2010.

Golterman, H. L.: Phosphate release from anoxic sediments or "What did Mortimer really write?", Hydrobiologia, 450(1-3), 745 99-106, https://doi.org/10.1023/A:1017559903404, 2001.

Govin, A., Holzwarth, U., Heslop, D., Ford Keeling, L., Zabel, M., Mulitza, S., Collins, J. A., and Chiessi, C. M.: Distribution of major elements in Atlantic surface sediments (36 N - 49 S): Imprint of terrigenous input and continental weathering, Geochem. Geophy. Geosy., 13(1), Q01013, https://doi.org/10.1029/2011GC003785, 2012.

Hasegawa, H., Tada, R., Jiang, X., Suganuma, Y., Imsamut, S., Charusiri, P., Ichinnorov, N., and Khand, Y.: Drastic 750 shrinking of the Hadley circulation during the mid-Cretaceous Supergreenhouse, Clim. Past, 8(4), 1323-1337, https://doi.org/10.5194/cp-8-1323-2012, 2012.

Hay, W. W. and Floegel, S.: New thoughts about the Cretaceous climate and oceans, Earth-Sci. Rev., 115(4), 262-272, https://doi.org/10.1016/j.earscirev.2012.09.008, 2012.

Hochuli, P. A., Menegatti, A. P., Weissert, H., Riva, A., Erba, E., and Silva, I. P.: Episodes of high productivity and cooling 755 in the early Aptian Alpine Tethys, Geology, 27(7), 657-660, https://doi.org/10.1130/0091-7613(1999)027<0657:EOHPAC>2.3.CO;2, 1999.

Holland H. D.: The Chemistry of the Atmosphere and Oceans, Wiley, New York, USA, 1978.

Ingall, E. D.: Biogeochemistry: phosphorus burial, Nat. Geosci., 3(8), 521, https://doi.org/10.1038/ngeo926, 2010.

Ingall, E. and Jahnke, R.: Evidence for enhanced phosphorus regeneration from marine sediments overlain by oxygen
760 depleted waters, Geochim. Cosmochim. Ac., 58(11), 2571-2575, https://doi.org/10.1016/0016-7037(94)90033-7, 1994.

Jarvis, I., Burnett, W. C., Nathan, Y., Almbaydin, F. S. M., Attia, A. K. M., Castro, L. N., Flicoteaux, R., Ezzeldim Hilmy, M., Husain, V., Qutawnah, A. A., Serjani, A., and Zanin, Y. N.: Phosphorite geochemistry: state-of-the-art and environmental concerns, Eclogae Geol. Helv., 87(3), 643-700, 1994.

Jarvis, I. A. N., Gale, A. S., Jenkyns, H. C., and Pearce, M. A.: Secular variation in Late Cretaceous carbon isotopes: a new
765 $\delta^{13}C$ carbonate reference curve for the Cenomanian–Campanian (99.6–70.6 Ma), Geol. Mag., 143(5), 561-608, https://doi.org/10.1017/S0016756806002421, 2006.

Jarvis, I., Lignum, J. S., Gröcke, D. R., Jenkyns, H. C., and Pearce, M. A.: Black shale deposition, atmospheric CO_2 drawdown, and cooling during the Cenomanian-Turonian Oceanic Anoxic Event, Paleoceanography, 26(3), PA3201, https://doi.org/10.1029/2010PA002081, 2011.

770 Jenkyns, H. C.: Cretaceous anoxic events: from continents to oceans, J. Geol. Soc. London, 137(2), 171-188, https://doi.org/10.1029/2010pa002081,2011, 1980.

Jenkyns, H. C.: Evidence for rapid climate change in the Mesozoic–Palaeogene greenhouse world, Philos. T. Roy. Soc. A, 361(1810), 1885-1916, https://doi.org/10.1098/rsta.2003.1240, 2003.

Jenkyns, H. C.: Geochemistry of oceanic anoxic events, Geochem. Geophy. Geosy., 11(3),
775 https://doi.org/10.1029/2009GC002788, 2010.

Jenkyns, H. C., Dickson, A. J., Ruhl, M., and Van den Boorn, S. H.: Basalt-seawater interaction, the Plenus Cold Event, enhanced weathering and geochemical change: deconstructing Oceanic Anoxic Event 2 (Cenomanian–Turonian, Late Cretaceous), Sedimentology, 64(1), 16-43, https://doi.org/10.1111/sed.12305, 2017.

Katz, M. E., Wright, J. D., Miller, K. G., Cramer, B. S., Fennel, K., and Falkowski, P. G.: Biological overprint of the
780 geological carbon cycle, Mar. Geol., 217(3-4), 323-338, https://doi.org/10.1016/j.margeo.2004.08.005, 2005.

Keller, C. E., Hochuli, P. A., Weissert, H., Bernasconi, S. M., Giorgioni, M., and Garcia, T. I.: A volcanically induced climate warming and floral change preceded the onset of OAE1a (Early Cretaceous), Palaeogeogr. Palaeocl., 305(1-4), 43-49, https://doi.org/10.1016/j.palaeo.2011.02.011, 2011.

Kolonic, S., Wagner, T., Forster, A., Sinninghe Damsté, J. S., Walsworth-Bell, B., Erba, E., Turgeon, S., Brumsack, H.-J.,
785 Chellai, E. H., Tsikos, H., Kuhnt, W., and Kuypers, M. M. M.: Black shale deposition on the northwest African Shelf during the Cenomanian/Turonian oceanic anoxic event: Climate coupling and global organic carbon burial, Paleoceanography, 20(1), PA1006, https://org/10.1029/2003PA000950, 2005.

Kuhnt, W., Thurow, J., Wiedmann, J., and Herbin, J. P.: Oceanic anoxic conditions around the Cenomanian/Turonian Boundary and the response of the biota, in: Biogeochemistry of Black Shales (Vol. 60), edited by: Degens, E. T., Meyers, P.
790 A., and Brassell, S. C., Mitteilungen aus dem Geologischen Institut der Univ. Hamburg, Germany, 205–246, 1986.

Climate
of the Past
Discussions

Kuhnt, W., Herbin, J., Thurow, J., and Wiedemann, J.: Distribution of Cenomanian-Turonian organic facies in the western Mediterranean and along the adjacent Atlantic margin, in: Deposition of organic facies (Vol. 30), Amer Assoc Petroleum Geologists, 133-160, 1990.

Kuhnt, W., Nederbragt, A., and Leine, L.: Cyclicity of Cenomanian-Turonian organic-carbon-rich sediments in the Tarfaya
795   Atlantic coastal basin (Morocco), Cretaceous Res., 18(4), 587-601, https://doi.org/10.1006/cres.1997.0076, 1997.

Kuhnt, W., Luderer, F., Nederbragt, S., Thurow, J., and Wagner, T.: Orbital-scale record of the late Cenomanian–Turonian oceanic anoxic event (OAE-2) in the Tarfaya Basin (Morocco), Int. J. Earth Sci., 94(1), 147-159, https://doi.org/10.1007/s00531-004-0440-5, 2005.

Kuhnt, W., Holbourn, A., Gale, A., Chellai, E. H., and Kennedy, W. J.: Cenomanian sequence stratigraphy and sea-level
800   fluctuations in the Tarfaya Basin (SW Morocco), Geol. Soc. Am. Bull., 121(11-12), 1695-1710, https://doi.org/10.1130/B26418.1, 2009.

Kuhnt, W., Holbourn, A. E., Beil, S., Aquit, M., Krawczyk, T., Flögel, S., Chellai, E. H., and Jabour, H.: Unraveling the onset of Cretaceous Oceanic Anoxic Event 2 in an extended sediment archive from the Tarfaya-Laayoune Basin, Morocco, Paleoceanography, 32(8), 923-946, https://doi.org/10.1002/2017PA003146, 2017.

805   Kump, L. R.: Interpreting carbon-isotope excursions: Strangelove oceans, Geology, 19(4), 299-302, https://doi.org/10.1130/0091-7613(1991)019<0299:ICIESO>2.3.CO;2, 1991.

Kuypers, M. M., Pancost, R. D., and Damste, J. S. S.: A large and abrupt fall in atmospheric CO_2 concentration during Cretaceous times, Nature, 399(6734), 342, https://doi.org/10.1038/20659, 1999.

Larson, R. L.: Latest pulse of Earth: Evidence for a mid-Cretaceous superplume, Geology, 19(6), 547-550,
810   https://doi.org/10.1130/0091-7613(1991)019<0547:LPOEEF>2.3.CO;2, 1991.

Laskar, J., Robutel, P., Joutel, F., Gastineau, M., Correia, A. C. M., and Levrard, B.: A long-term numerical solution for the insolation quantities of the Earth, Astron. Astrophys., 428(1), 261-285, https://doi.org/10.1051/0004-6361:20041335, 2004.

Laskar, J., Fienga, A., Gastineau, M., and Manche, H.: La2010: a new orbital solution for the long-term motion of the Earth, Astron. Astrophys., 532, A89, https://doi.org/10.1051/0004-6361/201116836, 2011a.

815   Laskar, J., Gastineau, M., Delisle, J. B., Farrés, A., and Fienga, A.: Strong chaos induced by close encounters with Ceres and Vesta, Astron. Astrophys., 532, L4, https://doi.org/10.1051/0004-6361/201117504, 2011b.

Leine, L.: Geology of the Tarfaya oil shale deposit, Morocco, Geol. Mijnbouw, 65, 57-74, 1986.

Li, Y. X., Bralower, T. J., Montañez, I. P., Osleger, D. A., Arthur, M. A., Bice, D. M., Herbert, T. D., Erba, E., and Silva, I. P.: Toward an orbital chronology for the early Aptian oceanic anoxic event (OAE1a, ~120 Ma), Earth Planet. Sc. Lett.,
820   271(1-4), 88-100, https://doi.org/10.1016/j.epsl.2008.03.055, 2008.

Li, R., Xu, J., Li, X., Shi, Z., and Harrison, P. J.: Spatiotemporal variability in phosphorus species in the Pearl River Estuary: Influence of the river discharge, Scientific reports, 7(1), 13649, https://doi.org/10.1038/s41598-017-13924-w, 2017a.

Li, Y. X., Montanez, I. P., Liu, Z., and Ma, L.: Astronomical constraints on global carbon-cycle perturbation during Oceanic Anoxic Event 2 (OAE2), Earth Planet. Sc. Lett., 462, 35-46, https://doi.org/10.1016/j.epsl.2017.01.007, 2017b.

825 Lorenzen, J., Kuhnt, W., Holbourn, A., Flögel, S., Moullade, M., and Tronchetti, G.: A new sediment core from the Bedoulian (Lower Aptian) stratotype at Roquefort-La Bédoule, SE France. Cretaceous Res., 39, 6-16. https://doi.org/10.1016/j.cretres.2012.03.019, 2013.

Ma, C., Meyers, S. R., Sageman, B. B., Singer, B. S., and Jicha, B. R.: Testing the astronomical time scale for oceanic anoxic event 2, and its extension into Cenomanian strata of the Western Interior Basin (USA), Geol. Soc. Am. Bull., 126(7-
830 8), 974-989, https://doi.org/10.1130/B30922.1, 2014.

Mackenzie, F. T., Ver, L. M., and Lerman, A.: Century-scale nitrogen and phosphorus controls of the carbon cycle, Chem. Geol., 190(1-4), 13-32, https://doi.org/10.1016/S0009-2541(02)00108-0, 2002.

Malinverno, A., Erba, E., and Herbert, T. D.: Orbital tuning as an inverse problem: Chronology of the early Aptian oceanic anoxic event 1a (Selli Level) in the Cismon APTICORE, Paleoceanography, 25(2), PA2203,
835 https://doi.org/10.1029/2009PA001769, 2010.

Mann, M. E. and Lees, J. M.: Robust estimation of background noise and signal detection in climatic time series, Climatic change, 33(3), 409-445, https://doi.org/10.1007/BF00142586, 1996.

Masse, J.P., Bouaziz, S., Amon, E.O., Baraboshin, E., Tarkowski, R.A., Bergerat, F., Sandulescu, M., Platel, J.P., Canerot, J., and Guiraud, R.: Early Aptian (112-114 Ma), in: Atlas Peri-Tethys, Palaeogeographical Maps, edited by: Dercourt, J.,
840 Gaetani, M., and Vrielynck, B., CCGM, Paris, 119-127, 2000.

Masure, E., Raynaud, J. F., Pons, D., and de Reneville, P.: Palynologie du stratotype historique de l'Aptien inférieur dans la région de Cassis-La Bédoule (SE France), Géologie méditerranéenne, 25(3), 263-287, 1998.

Menegatti, A. P., Weissert, H., Brown, R. S., Tyson, R. V., Farrimond, P., Strasser, A., and Caron, M.: High-resolution δ13C stratigraphy through the early Aptian "Livello Selli" of the Alpine Tethys, Paleoceanography, 13(5), 530-545,
845 https://doi.org/10.1029/98PA01793, 1998.

Meyers, S. R.: Astrochron: An R package for astrochronology, https://cran.r-project.org/package=astrochron, 2014.

Meyers, S. R., and Sageman, B. B.: Quantification of deep-time orbital forcing by average spectral misfit, Am. J. Sci., 307(5), 773-792, https://doi.org/10.2475/05.2007.01, 2007.

Meyers, S. R., Sageman, B. B., and Arthur, M. A.: Obliquity forcing of organic matter accumulation during Oceanic Anoxic
850 Event 2, Paleoceanography, 27(3), PA3212, https://doi.org/10.1029/2012PA002286, 2012a.

Meyers, S. R., Siewert, S. E., Singer, B. S., Sageman, B. B., Condon, D. J., Obradovich, J. D., Jicha, B. R., and Sawyer, D. A.: Intercalibration of radioisotopic and astrochronologic time scales for the Cenomanian-Turonian boundary interval, Western Interior Basin, USA, Geology, 40(1), 7-10, https://doi.org/10.1130/G32261.1, 2012b.

Mort, H. P., Adatte, T., Föllmi, K. B., Keller, G., Steinmann, P., Matera, V., Berner, Z., and Stüben, D.: Phosphorus and the
855 roles of productivity and nutrient recycling during oceanic anoxic event 2, Geology, 35(6), 483-486, https://doi.org/10.1130/G23475A.1, 2007.

Mort, H. P., Adatte, T., Keller, G., Bartels, D., Föllmi, K. B., Steinmann, P., Berner, Z., and Chellai, E. H.: Organic carbon deposition and phosphorus accumulation during Oceanic Anoxic Event 2 in Tarfaya, Morocco, Cretaceous Res., 29(5-6), 1008-1023, https://doi.org/10.1016/j.cretres.2008.05.026, 2008.

860 Moullade, M., Tronchetti, G., Granier, B., Bornemann, A., Kuhnt, W., and Lorenzen, J.: High-resolution integrated stratigraphy of the OAE1a and enclosing strata from core drillings in the Bedoulian stratotype (Roquefort-La Bédoule, SE France), Cretaceous Res., 56, 119-140, https://doi.org/10.1016/j.cretres.2015.03.004, 2015.

Mulitza, S., Prange, M., Stuut, J. B., Zabel, M., von Dobeneck, T., Itambi, A. C., Nizou, J., Schulz, M., and Wefer, G.: Sahel megadroughts triggered by glacial slowdowns of Atlantic meridional overturning, Paleoceanography, 23(4), PA4206,
865 https://doi.org/10.1029/2008PA001637, 2008.

Nederbragt, A. J., Thurow, J., Vonhof, H., and Brumsack, H. J.: Modelling oceanic carbon and phosphorus fluxes: implications for the cause of the late Cenomanian Oceanic Anoxic Event (OAE2), J. Geol. Soc. London, 161(4), 721-728, https://doi.org/10.1144/0016-764903-075, 2004.

Niebuhr, B.: Geochemistry and time-series analyses of orbitally forced Upper Cretaceous marl–limestone rhythmites (Lehrte
870 West Syncline, northern Germany), Geol. Mag., 142(1), 31-55, https://doi.org/10.1017/S0016756804009999, 2005.

Noffke, A., Hensen, C., Sommer, S., Scholz, F., Bohlen, L., Mosch, T., Graco, M. and Wallmann, K.: Benthic iron and phosphorus fluxes across the Peruvian oxygen minimum zone, Limnol. Oceanogr., 57(3), 851-867, https://doi.org/10.4319/lo.2012.57.3.0851, 2012.

O'Brien, C. L., Robinson, S. A., Pancost, R. D., Damste, J. S. S., Schouten, S., Lunt, D. J., Alsenz, H., Bornemann, A.,
875 Bottini, C., Brassell, S. C., Farnsworth, A., Forster, A., Huber, B. T., Inglis, G. N., Jenkyns, H. C., Linnert, C., Littler, K., Markwick, P., McAnena, A., Mutterlose, J., Naafs, D. A., Püttmann, W., Sluijs, A., van Helmond, N. A. G. M., Vellekoop, J., Wagner, T., and Wrobel, N. E.: Cretaceous sea-surface temperature evolution: Constraints from TEX86 and planktonic foraminiferal oxygen isotopes, Earth-Sci. Rev., 172, 224-247, https://doi.org/10.1016/j.earscirev.2017.07.012, 2017.

Oxmann, J. F., Pham, Q. H., and Lara, R. J.: Quantification of individual phosphorus species in sediment: a sequential
880 conversion and extraction method, Eur. J. Soil Sci., 59(6), 1177-1190, https://doi.org/10.1111/j.1365-2389.2008.01062.x, 2008.

Pälike, H., Norris, R. D., Herrle, J. O., Wilson, P. A., Coxall, H. K., Lear, C. H., Shackleton, N. J., Tripati, A. K., and Wade, B. S.: The heartbeat of the Oligocene climate system, Science, 314(5807), 1894-1898, https://doi.org/10.1126/science.1133822, 2006.

885 Patterson, M. O., McKay, R., Naish, T., Escutia, C., Jimenez-Espejo, F. J., Raymo, M. E., Meyers, S. R., Tauxe, L., Brinkhuis, H., and IODP Expedition 318 Scientists: Orbital forcing of the East Antarctic ice sheet during the Pliocene and Early Pleistocene, Nat. Geosci., 7(11), 841, https://doi.org/10.1038/ngeo2273, 2014.

Peterson, L. C., Haug, G. H., Hughen, K. A., and Röhl, U.: Rapid changes in the hydrologic cycle of the tropical Atlantic during the last glacial, Science, 290(5498), 1947-1951, https://doi.org/10.1126/science.290.5498.1947, 2000.

890 Petrizzo, M. R., Huber, B. T., Wilson, P. A., and MacLeod, K. G.: Late Albian paleoceanography of the western subtropical North Atlantic, Paleoceanography, 23(1), PA1213, https://doi.org/10.1029/2007PA001517, 2008.

R Core Team: R: A language and environment for statistical computing. R Foundation for Statistical Computing, Vienna, Austria. https://www.R-project.org/, 2018.

Reboulet, S., Giraud, F., Colombié, C., and Carpentier, A.: Integrated stratigraphy of the Lower and Middle Cenomanian in a
895 Tethyan section (Blieux, southeast France) and correlations with Boreal basins, Cretaceous Res., 40, 170-189, https://doi.org/10.1016/j.cretres.2012.06.006, 2013.

Redfield, A. C.: The biological control of chemical factors in the environment, Am. Sci., 46(3), 230A-221, 1958.

Redfield, A. C.: The influence of organisms on the composition of seawater, in: The sea, edited by Hill, M. N., Interscience, New York, USA, 2, 26-77, 1963.

900 Riggs, S. R.: Phosphorite sedimentation in Florida - a model phosphogenic system, Econ. Geol., 74, 285–314, https://doi.org/10.2113/gsecongeo.74.2.285, 1979.

Roth, R., Ritz, S. P., and Joos, F.: Burial-nutrient feedbacks amplify the sensitivity of atmospheric carbon dioxide to changes in organic matter remineralisation, Earth syst. Dynam., 5(2), 321-343, https://doi.org/10.5194/esd-5-321-2014, 2014.

Ruttenberg, K. C.: Reassessment of the oceanic residence time of phosphorus, Chem. Geol., 107, 405–409,
905 https://doi.org/10.1016/0009-2541(93)90220-D, 1993.

Ruttenberg, K. C.: The Global Phosphorus Cycle, in: Treatise on Geochemistry (Vol. 8), edited by Turekian, K. K. and Holland, H. D., Elsevier, 585–643, https://doi.org/10.1016/B0-08-043751-6/08153-6, 2003.

Ruttenberg, K. C. and Berner, R. A.: Authigenic apatite formation and burial in sediments from non-upwelling continental margins, Geochim. Cosmochimica Ac., 57, 991–1007, https://doi.org/10.1016/0016-7037(93)90035-U, 1993.

910 Sageman, B. B., Meyers, S. R., and Arthur, M. A.: Orbital time scale and new C-isotope record for Cenomanian-Turonian boundary stratotype, Geology, 34(2), 125-128, https://doi.org/10.1130/G22074.1, 2006.

Schlanger, S. O. and Jenkyns, H. C.: Cretaceous oceanic anoxic events: causes and consequences, Geol. mijnbouw, 55(3-4), 179-184.

Schlanger, S. O., Jenkyns, H. C., and Premoli-Silva, I.: Volcanism and vertical tectonics in the Pacific Basin related to global
915 Cretaceous transgressions, Earth Planet. Sc. Lett., 52(2), 435-449, https://doi.org/10.1016/0012-821X(81)90196-5, 1981.

Schlanger, S. O., Arthur, M. A., Jenkyns, H. C., and Scholle, P. A.: The Cenomanian-Turonian Oceanic Anoxic Event, I. Stratigraphy and distribution of organic carbon-rich beds and the marine δ^{13}C excursion, Geol. Soc. (London) Spec Publ, 26(1), 371-399, https://doi.org/10.1144/GSL.SP.1987.026.01.24, 1987.

Schroller-Lomnitz, U., Hensen, C., Dale, A. W., Scholz, F., Clemens, D., Sommer, S., Noffke, A., and Wallmann, K.:
920 Dissolved benthic phosphate, iron and carbon fluxes in the Mauritanian upwelling system and implications for ongoing deoxygenation, Deep-Sea Res. Part I, 143, 70-84, https://doi.org/10.1016/j.dsr.2018.11.008, 2019.

Scholz, F., Beil, S., Flögel, S., Lehmann, M. F., Holbourn, A., Wallmann, K., and Kuhnt, W.: Oxygen minimum zone-type biogeochemical cycling in the Cenomanian-Turonian Proto-North Atlantic across Oceanic Anoxic Event 2. Earth Planet. Sc. Lett., 517, 50-60, https://doi.org/10.1016/j.epsl.2019.04.008, 2019.

925 Schulz, H. N. and Schulz, H. D.: Large sulfur bacteria and the formation of phosphorite, Science, 307(5708), 416-418, https://doi.org/10.1126/science.1103096, 2005.

Scott, R. W.: A Cretaceous chronostratigraphic database: construction and applications, Carnets geol., 14(2), 15-37, https://doi.org/10.4267/2042/53522, 2014.

Slomp, C. P. and Van Cappellen, P.: The global marine phosphorus cycle: sensitivity to oceanic circulation, Biogeosciences,
930 3(5), 1587-1629, http://doi.org/10.5194/bg-4-155-2007, 2007.

Slomp C. P., Epping E. H. G., Helder W., and Van Raaphorst W.: A key role for iron-bound phosphorus in authigenic apatite formation in North Atlantic continental platform sediments, J. Mar. Res., 54, 1179–1205, https://doi.org/10.1357/0022240963213745, 1996a.

Slomp, C. P., Van der Gaast, S. J., and Van Raaphorst W.: Phosphorus binding by poorly crystalline iron oxides in North Sea
935 sediments, Mar. Chem., 52, 55–73, https://doi.org/10.1016/0304-4203(95)00078-X, 1996b.

Slomp, C. P., Thomson, J., and de Lange, G. J.: Controls on phosphorus regeneration and burial during formation of eastern Mediterranean sapropels, Mar. Geol., 203(1-2), 141-159, https://doi.org/10.1016/S0025-3227(03)00335-9, 2004.

Smith, S. V.: Phosphorus versus nitrogen limitation in the marine environment, Limnol. Oceanogr., 29(6), 1149-1160, https://doi.org/10.4319/lo.1984.29.6.1149, 1984.

940 Stein, M., Föllmi, K. B., Westermann, S., Godet, A., Adatte, T., Matera, V., Fleitmann, D., and Berner, Z.: Progressive palaeoenvironmental change during the late Barremian–early Aptian as prelude to Oceanic Anoxic Event 1a: Evidence from the Gorgo a Cerbara section (Umbria-Marche basin, central Italy), Palaeogeogr. Palaeocl., 302(3-4), 396-406, https://doi.org/10.1016/j.palaeo.2011.01.025, 2011.

Thomson, D. J.: Spectrum estimation and harmonic analysi,. P. IEEE, 70(9), 1055-1096,
945 https://doi.org/10.1109/PROC.1982.12433, 1982.

Tisserand, A., Malaizé, B., Jullien, E., Zaragosi, S., Charlier, K., and Grousset, F.: African monsoon enhancement during the penultimate glacial period (MIS 6.5 ∼170 ka) and its atmospheric impact, Paleoceanography, 24(2), PA2220, https://doi.org/10.1029/2008PA001630, 2009.

Trabucho-Alexandre, J., Tuenter, E., Henstra, G. A., van der Zwan, K. J., van de Wal, R. S., Dijkstra, H. A., and de Boer, P.
950 L.: The mid-Cretaceous North Atlantic nutrient trap: black shales and OAEs, Paleoceanography, 25(4), PA4201, https://doi.org/10.1029/2010PA001925, 2010.

Tsikos, H., Jenkyns, H. C., Walsworth-Bell, B., Petrizzo, M. R., Forster, A., Kolonic, S., Erba, E., Premoli Silva, I., Baas, M., Wagner, T., and Sinninghe Damsté, J. S.: Carbon-isotope stratigraphy recorded by the Cenomanian–Turonian Oceanic Anoxic Event: correlation and implications based on three key localities, J. Geol. Soc. London, 161(4), 711-719,
955 https://doi.org/10.1144/0016-764903-077, 2004.

Turgeon, S. C. and Creaser, R. A.: Cretaceous oceanic anoxic event 2 triggered by a massive magmatic episode, Nature, 454(7202), 323, https://doi.org/10.1038/nature07076, 2008.

Tyrrell, T.: The relative influences of nitrogen and phosphorus on oceanic primary production, Nature, 400, 525-531, https://doi.org/10.1038/22941, 1999.

960 van Bentum, E. C., Reichart, G. J., Forster, A., and Sinninghe Damsté, J. S.: Latitudinal differences in the amplitude of the OAE-2 carbon isotopic excursion: pCO$_2$ and paleo productivity, Biogeosciences, 9(2), 717-731, https://doi.org/10.5194/bg-9-717-2012, 2012.

Voigt, S., Gale, A. S., and Flögel, S.: Midlatitude shelf seas in the Cenomanian-Turonian greenhouse world: Temperature evolution and North Atlantic circulation, Paleoceanography, 19(4), PA4020, https://doi.org/10.1029/2004PA001015, 2004.

965 Wagner, T., Wallmann, K., Herrle, J. O., Hofmann, P., and Stuesser, I.: Consequences of moderate ~25,000 yr lasting emission of light CO$_2$ into the mid-Cretaceous ocean, Earth Planet. Sc. Lett., 259(1-2), 200-211, https://doi.org/10.1016/j.epsl.2007.04.045, 2007.

Wallmann, K.: Feedbacks between oceanic redox states and marine productivity: A model perspective focused on benthic phosphorus cycling, Global Biogeochem. Cy., 17(3), 10, https://doi.org/10.1029/2002GB001968, 2003.

970 Wallmann, K.: Phosphorus imbalance in the global ocean?, Global Biogeochem. Cy., 24(4), GB4030. https://doi.org/10.1029/2009GB003643, 2010.

Weaver, C. E.: Potassium, illite and the ocean, Geochim. Cosmochim. ac., 31(11), 2181-2196, https://doi.org/10.1016/0016-7037(67)90060-9, 1967.

Weaver, C. E. Developments in Sedimentology 44 - Clays, muds, and shales, Elsevier, 1989.

975 Weltje, G. J. and Tjallingii, R.: Calibration of XRF core scanners for quantitative geochemical logging of sediment cores: theory and application, Earth and Plan. Sc. Lett., 274(3-4), 423-438, https://doi.org/10.1016/j.epsl.2008.07.054, 2008.

Wendler, I.: A critical evaluation of carbon isotope stratigraphy and biostratigraphic implications for Late Cretaceous global correlation, Earth-Sci. Rev., 126, 116-146, https://doi.org/10.1016/j.earscirev.2013.08.003, 2013.

Wilson, J.: Did the Atlantic close and then reopen?, Nature, 211, 676-681, https://doi.org/10.1038/211676a0, 1966.

980 Worsley, T. R., Nance, R. D., and Moody, J. B.: Tectonic cycles and the history of the Earth's biogeochemical and paleoceanographic record, Paleoceanography, 1(3), 233-263, https://doi.org/10.1029/PA001i003p00233, 1986.

Yao, H., Chen, X., Melinte-Dobrinescu, M. C., Wu, H., Liang, H., and Weissert, H.: Biostratigraphy, carbon isotopes and cyclostratigraphy of the Albian-Cenomanian transition and Oceanic Anoxic Event 1d in southern Tibet, Palaeogeogr. Palaeocl., 499, 45-55, https://doi.org/10.1016/j.palaeo.2018.03.005, 2018.

985

Table 1. Durations of major Cretaceous OAEs.

Carbon isotope excursion	Time interval	Duration	Estimate for	Publication
OAE1a	early Aptian to late Aptian	~1.0–1.3 Myr	Carbon isotope stage C3 to C6 of Menegatti et al. (1998) in $\delta^{13}C$	Li et al. (2008)
		1.11 ±0.11 Myr	Selli Level	Malinverno et al. (2010)
		1.36 Myr	increase to inflection point of $\delta^{13}C$	Scott (2014)
		1.157 Myr	Carbon isotope stage C3 to C6 of Menegatti et al. (1998)	Moullade et al. (2015)
OAE1b	late Aptian to Early Albian	~210 kyr	Positive isotope excursion in $\delta^{13}C$	Erbacher et al. (2001)
		46 kyr	black shale deposition	
		45 kyr	negative excursion and increase to $\delta^{13}C$ maximum	Wagner et al. (2007)
		40 kyr	Positive isotope excursion in $\delta^{13}C$	
		1.84 Myr		Scott (2014)
OAE1c	middle Albian	1.01 Myr	increase to $\delta^{13}C$ maximum	Scott (2014)
OAE1d	Albian – Cenomanian boundary interval	400 kyr	increase to $\delta^{13}C$ maximum	Petrizzo et al. (2008)
		ca 1 Myr	ACBI (Albian-Cenomanian boundary interval) from the onset of peak A (OAE1d) to the return to background values after peak D in $\delta^{13}C$	Bornemann et al. (2017)
		1.21 ±0.17 Myr	OAE1d from the onset of peak A to peak C in $\delta^{13}C$	Gambacorta et al. (2019)
		~233 kyr	onset and peak phase in $\delta^{13}C$	Yao et al. (2018)
		0.4 Myr	increase to inflection point in $\delta^{13}C$	Scott (2014)
MCE	Mid-Cenomanian	~200 kyr	onset to second peak in $\delta^{13}C$	Voigt et al. (2004)
		less than 400 kyr	onset to second peak in $\delta^{13}C$	Reboulet et al. (2013)
		210 kyr	onset until return to background values in $\delta^{13}C$	Eldrett et al. (2015)

| OAE2	Cenomanian – Turonian boundary interval	563 to 601 kyr	Onset, peak and plateau phase in $\delta^{13}C$	Sageman et al. (2006)
		847 to 885 kyr	Onset, peak, plateau phase and recovery phase in $\delta^{13}C$	
		450–500 kyr	in S13 (Tarfaya Basin) between onset and end of plateau in $\delta^{13}C$	Meyers et al. (2012a)
		500–550 kyr	in 1261B (Demerara Rise) between onset and end of plateau in $\delta^{13}C$	
		516–613 kyr	in the Angus Core (Western Interior Seaway); Onset, peak, plateau phase and recovery phase in $\delta^{13}C$	Ma et al. (2014)
		559–675 kyr	in the Portland Core (Western Interior Seaway); Onset, peak, plateau phase and recovery phase in $\delta^{13}C$	
		0.52 Myr	onset phase in $\delta^{13}C$	Scott (2014)
		0.71 ±0.17 Myr	onset until end of plateau phase in $\delta^{13}C$	Eldrett et al. (2015)
		0.92 ±0.17 Myr	Negative excursion, onset, peak and plateau phase in $\delta^{13}C$	
		650 ±25 kyr	onset until end of plateau phase in $\delta^{13}C$	Li et al. (2017b)
		~820 kyr	Onset, peak, plateau phase and recovery phase in $\delta^{13}C$	
		~675 kyr	onset until end of plateau phase in $\delta^{13}C$	Charbonnier et al. (2018)
		~956 kyr	Onset, peak, plateau phase and recovery phase in $\delta^{13}C$	

990
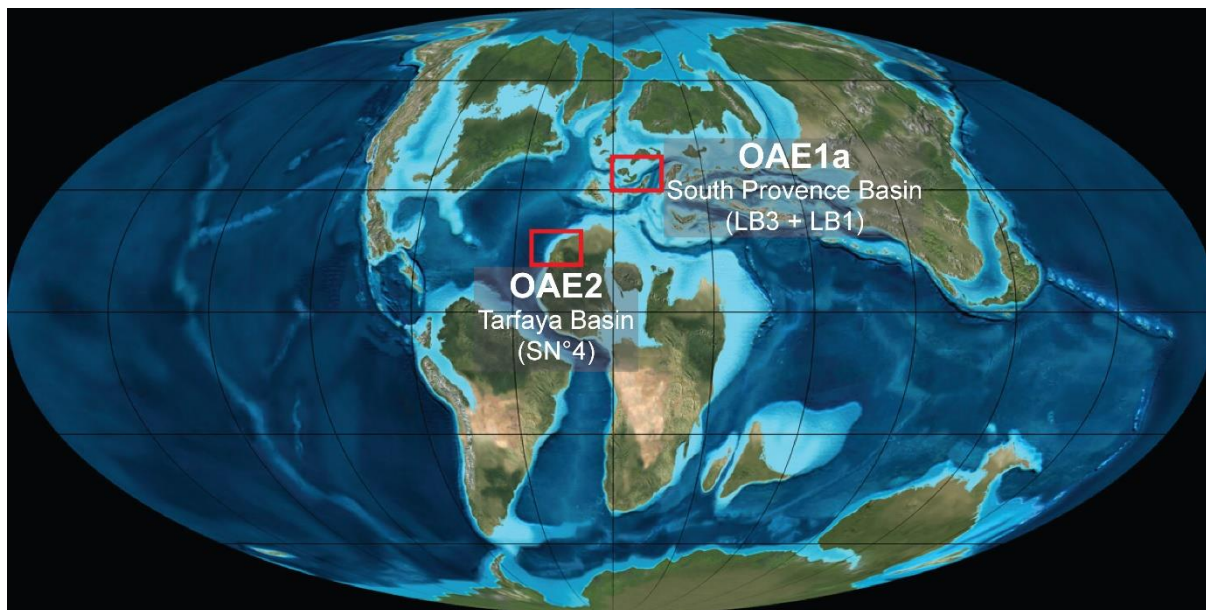
Fig. 1. Reconstruction of Late Cretaceous paleogeography at 100 Ma (Ron Blakey, Colorado Plateau Geosystems). Red boxes indicate locations of South Provence and Tarfaya Basins.
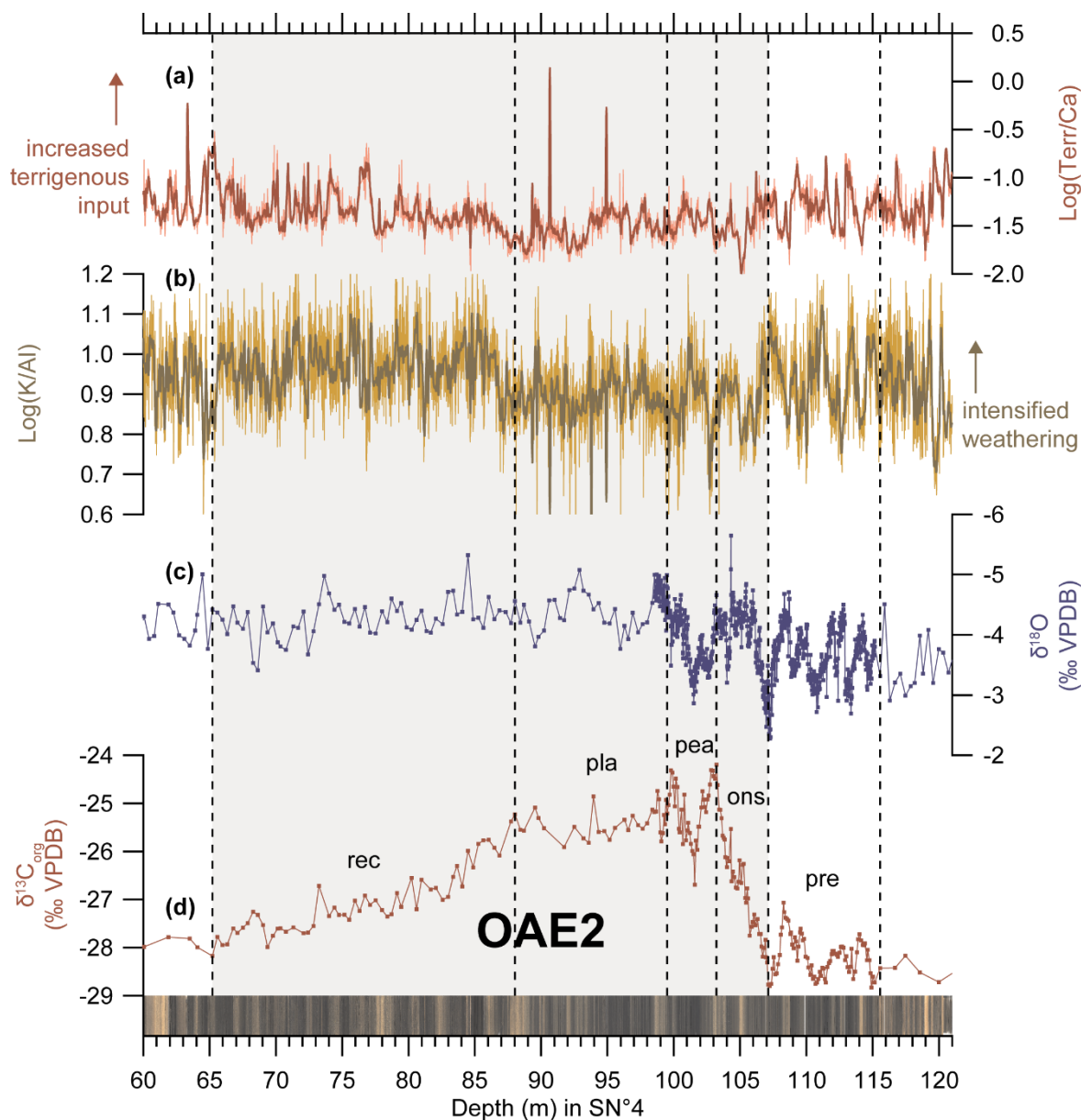
Fig. 2. Linescan photographs, stable isotope and XRF-scanning elemental records spanning OAE2 in Tarfaya Basin Core SN°4. **(a)** Log(Terr/Ca) from Kuhnt et al. (2017) and Beil et al. (2018). **(b)** Log(K/Al) from Kuhnt et al. (2017) and Beil et al. (2018). **(c)** $\delta^{13}O$ and **(d)** $\delta^{13}C_{org}$ from Kuhnt et al. (2017) and Beil et al. (2018). The phases of OAE2 are indicated as vertical black dashed lines and marked with abbreviations for precursor (pre), onset (ons), peak (pea), plateau (pla) and recovery (rec) phases.
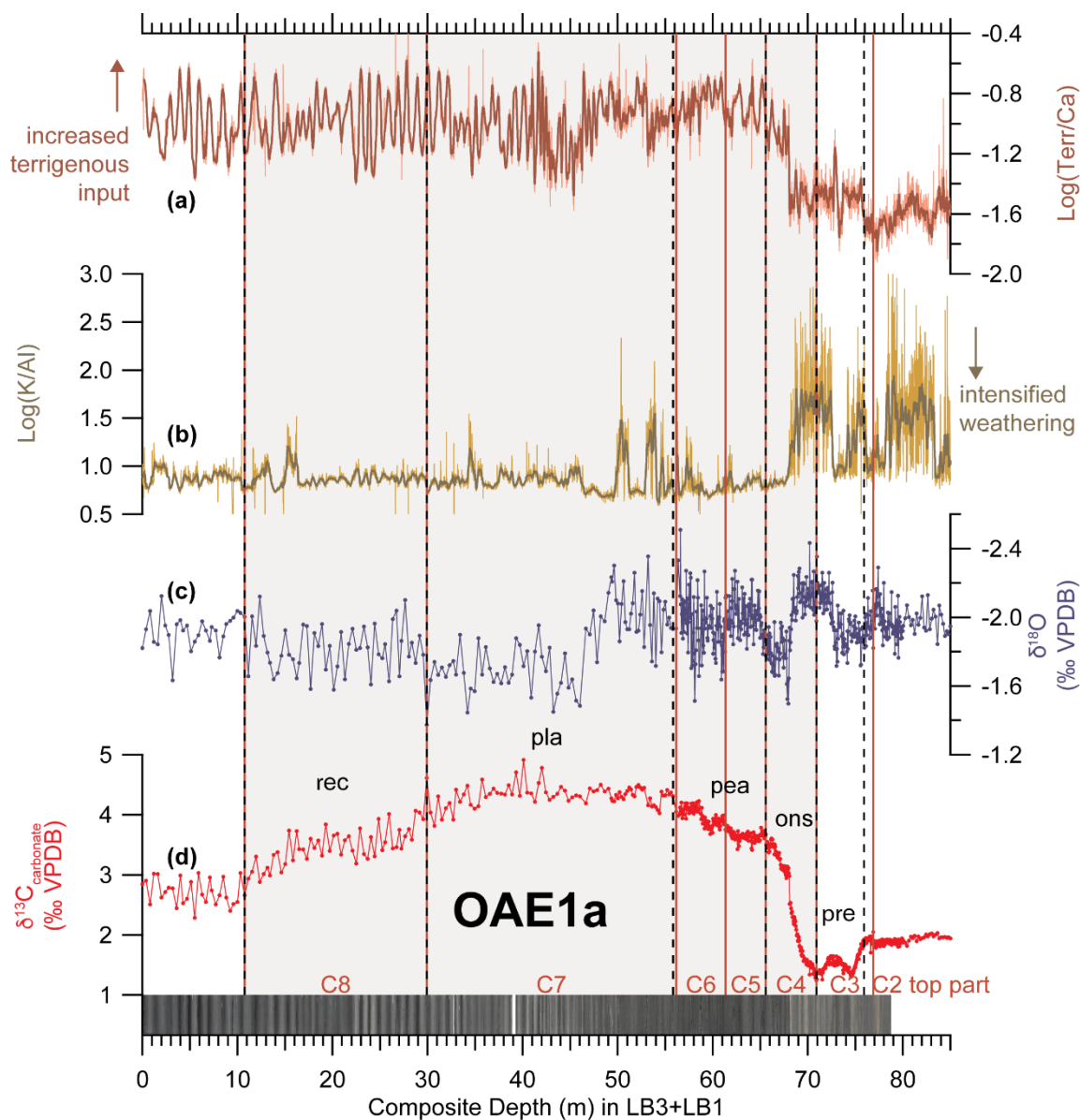
Fig. 3. Linescan photographs, stable isotope and XRF-scanning elemental records spanning OAE1a from Core LB3LB1. **(a)** Log(Terr/Ca). **(b)** Log(K/Al). **(c)** δ^{13}O and **(d)** $\delta^{13}C_{carbonate}$ from Lorenzen et al. (2013) and Moullade et al. (2015) with new high-resolution isotope data from this study. The phases of OAE1a are indicated by vertical black dashed lines and marked with precursor (pre), onset (ons), peak (pea), plateau (pla) and recovery (rec) phase, carbon isotope stages of Menegatti et al. (1998) are indicated by vertical red lines.
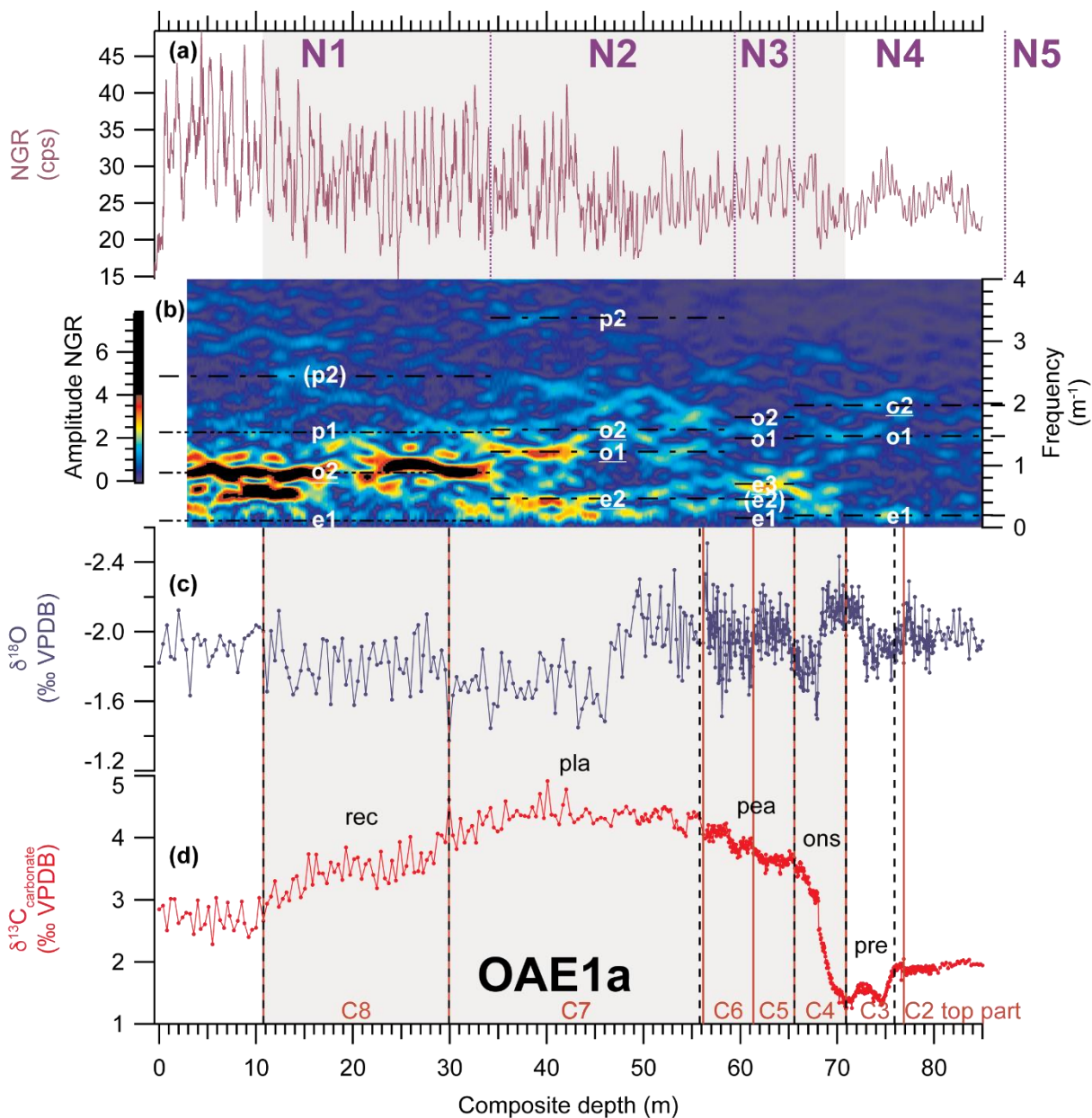
Fig. 4. Natural Gamma Ray (NGR) and stable isotope records and Evolutive Harmonic Analysis (EHA) of NGR spanning OAE1a from Core LB3LB1. **(a)** NGR. **(b)** EHA plot of NGR with correlated orbital periodicities indicated by dashed black lines and labelled in white. **(c)** $\delta^{18}O$ and **(d)** $\delta^{13}C_{carbonate}$ from Lorenzen et al. (2013) and Moullade et al. (2015) with new high-resolution isotope data from this study. Dashed vertical lines and numbers in purple on top indicate intervals for power spectral analysis. Carbon isotope stages of Menegatti et al. (1998) are indicated by vertical red lines and numbers at the bottom. The phases of OAE1a are indicated by vertical black dashed lines and marked with precursor (pre), onset (ons), peak (pea), plateau (pla) and recovery (rec) phase. Note: the colorscheme of the EHA-diagram is limited to 50% to limit the effect of the top-interval with high power in singular frequencies and thereby enhance the visibility in the lower part of the core, characterized by multiple frequencies with lower power.

1020 **Table 2.** Durations and sedimentation rates for Aptian C-stages of Menegatti et al. (1998) and comparison with durations of Malinverno et al. (2010).

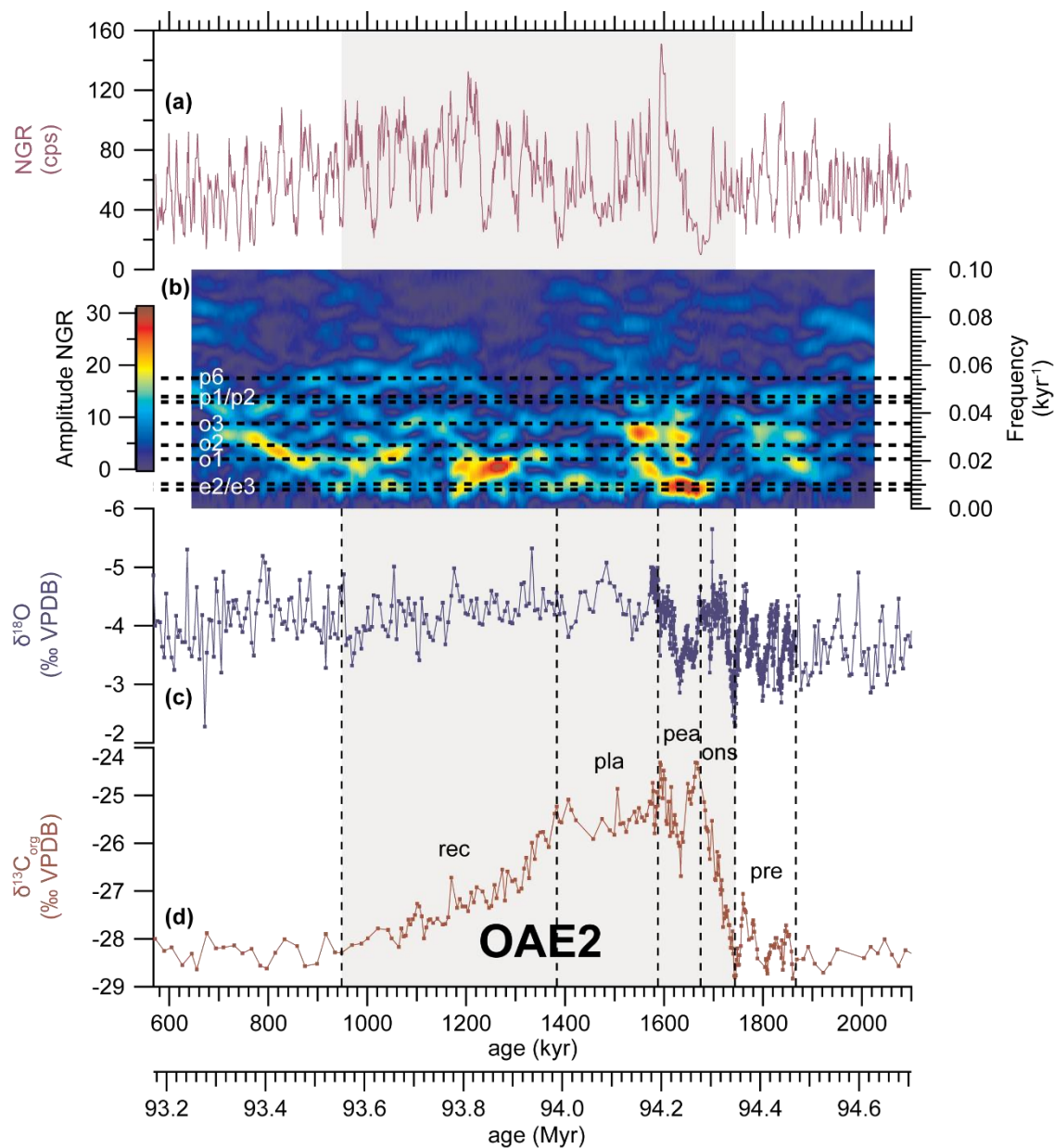| C-stage	top in LB3/LB1 (m)	bottom in LB3/LB1 (m)	segment	total duration (kyr)	mean SedRate during C-stage (cm kyr^{-1})	durations (kyr) of Malinverno et al. (2010)
C8	10.75	29.92	N1	625	3.07	
C7	29.92	56.16	N1 + N2	1398	1.88	1590
C6	56.16	61.35	N2 + N3	315	1.65	349
C5	61.35	65.58	N3	281	1.50	510
C4	65.58	70.91	N4	388	1.37	239
C3	70.91	76.87	N4	434	1.37	46.7

Fig. 5. Natural Gamma Ray (NGR) and stable isotope records and Evolutive Harmonic Analysis (EHA) of NGR spanning OAE2 in Core SN°4. **(a)** NGR. **(b)** EHA plot of NGR with orbital periodicities indicated as dashed black lines and labelled in white. **(c)** δ^{18}O and **(d)** $\delta^{13}C_{org}$ from Kuhnt et al. (2017) and Beil et al. (2018). The phases of OAE2 are indicated by vertical black dashed lines and marked with precursor (pre), onset (ons), peak (pea), plateau (pla) and recovery (rec) phase.
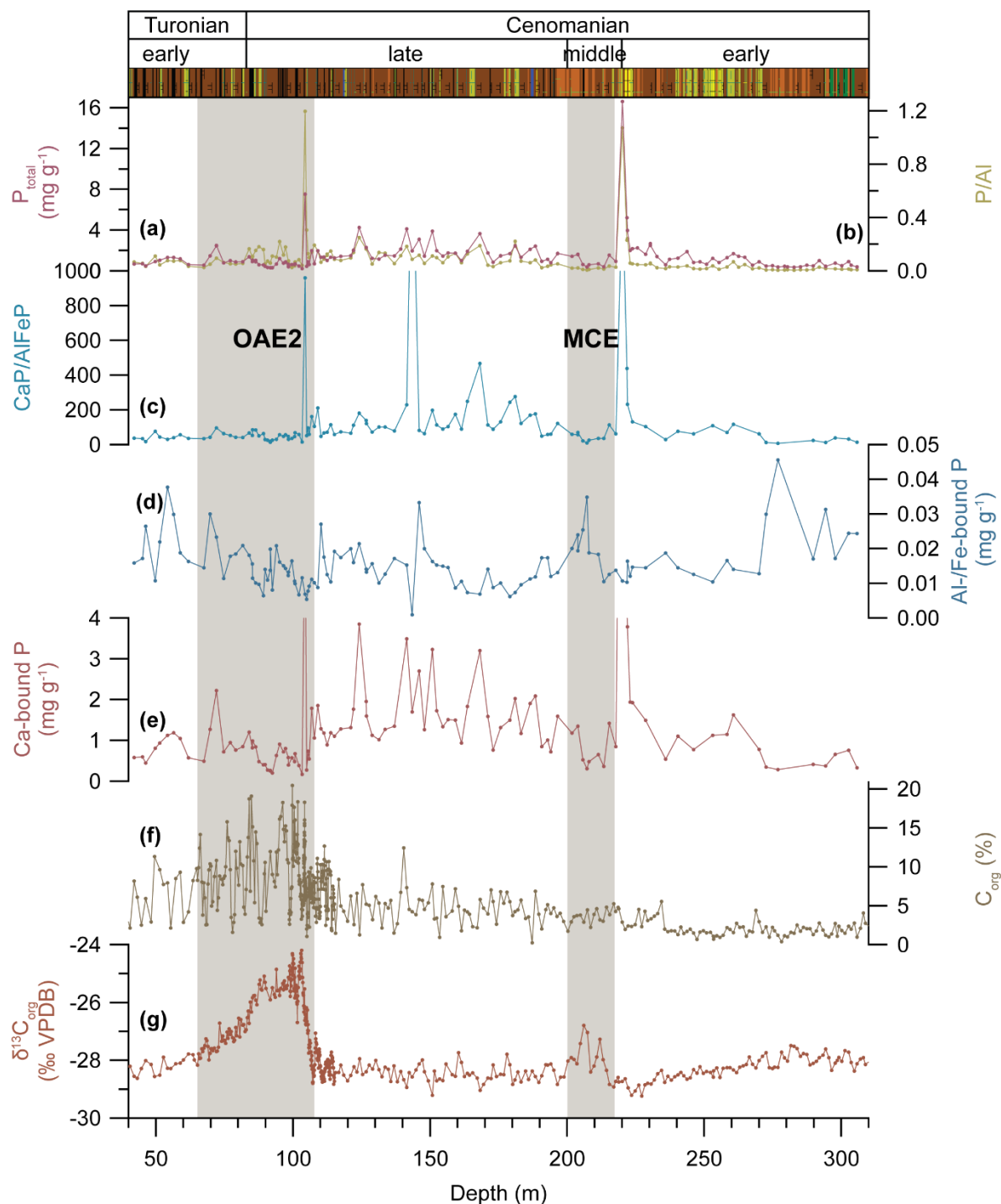
Fig. 6. Phosphorus concentration and speciation in Core SN°4. **(a)** Concentration of total phosphorus (P_{total}). **(b)** ratio of total phosphorus to aluminium (P/Al) measured on bulk sediment. **(c)** ratio of calcium- to aluminium/iron-bound phosphorus (CaP/AlFeP). **(d)** concentration of aluminium/iron bound-phosphorus (Al-/Fe-bound P). **(e)** concentration of calcium-bound phosphorus (Ca-bound P). **(f)** concentration of organic carbon (C_{org}) and **(g)** $\delta^{13}C_{org}$ from Kuhnt et al. (2017) and Beil et al. (2018).
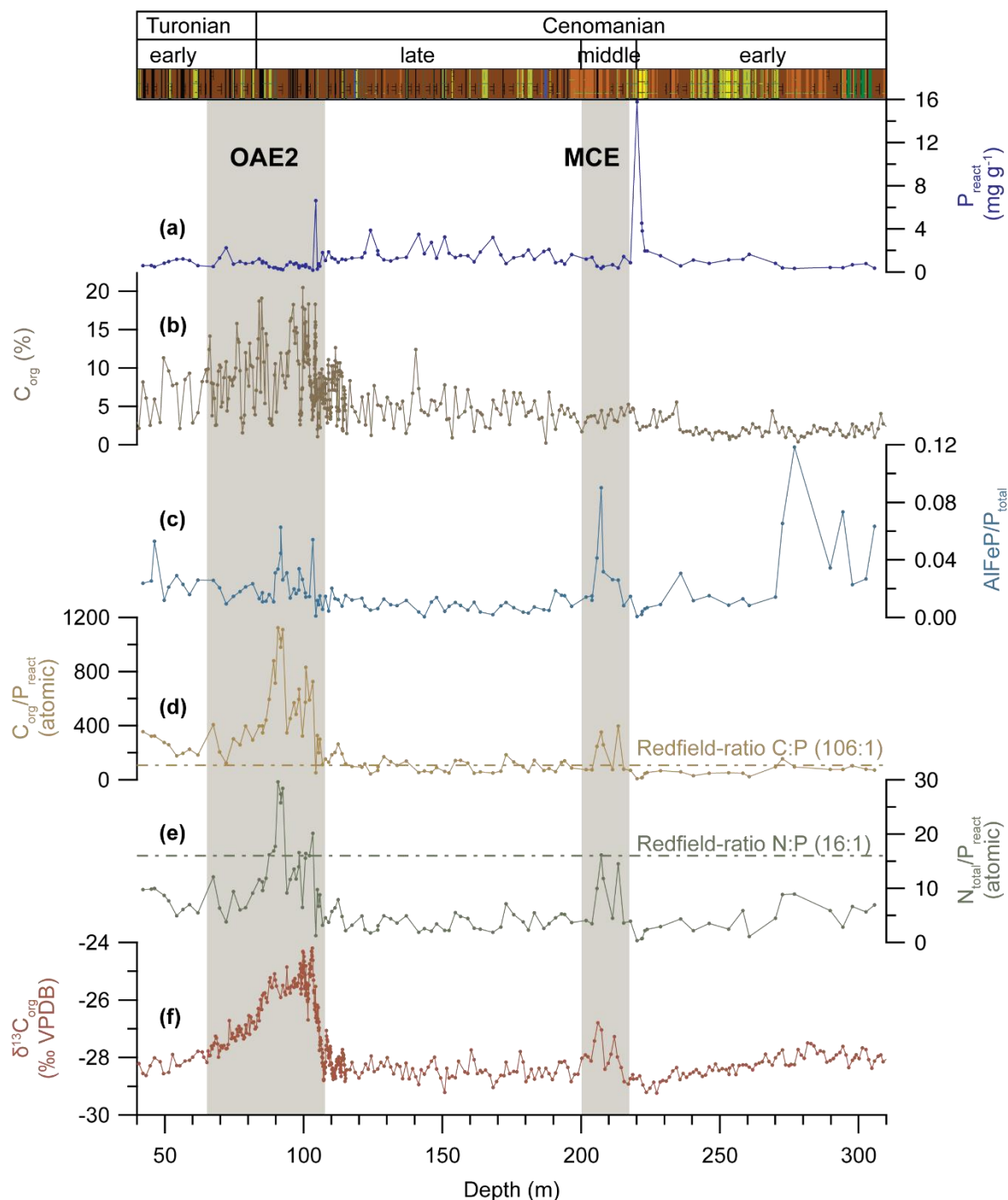
Fig. 7. Phosphorus speciation in Core SN°4. **(a)** concentration of reactive phosphorus calculated as the sum of Al-/Fe- and Ca-bound P (P_{react}). **(b)** concentration of organic carbon (C_{org}). **(c)** ratio of aluminium and iron bound phosphorus to total phosphorus ($AlFeP/P_{total}$). **(d)** atomic ratio of organic carbon to reactive phosphorus (C_{org}/P_{react}) with Redfield ratio 106:1 indicated as dashed line. **(e)** atomic ratio of total nitrogen to reactive phosphorus (N_{total}/P_{react}) with Redfield ratio 16:1 indicated as dashed line. **(f)** $\delta^{13}C_{org}$ from Kuhnt et al. (2017) and Beil et al. (2018).
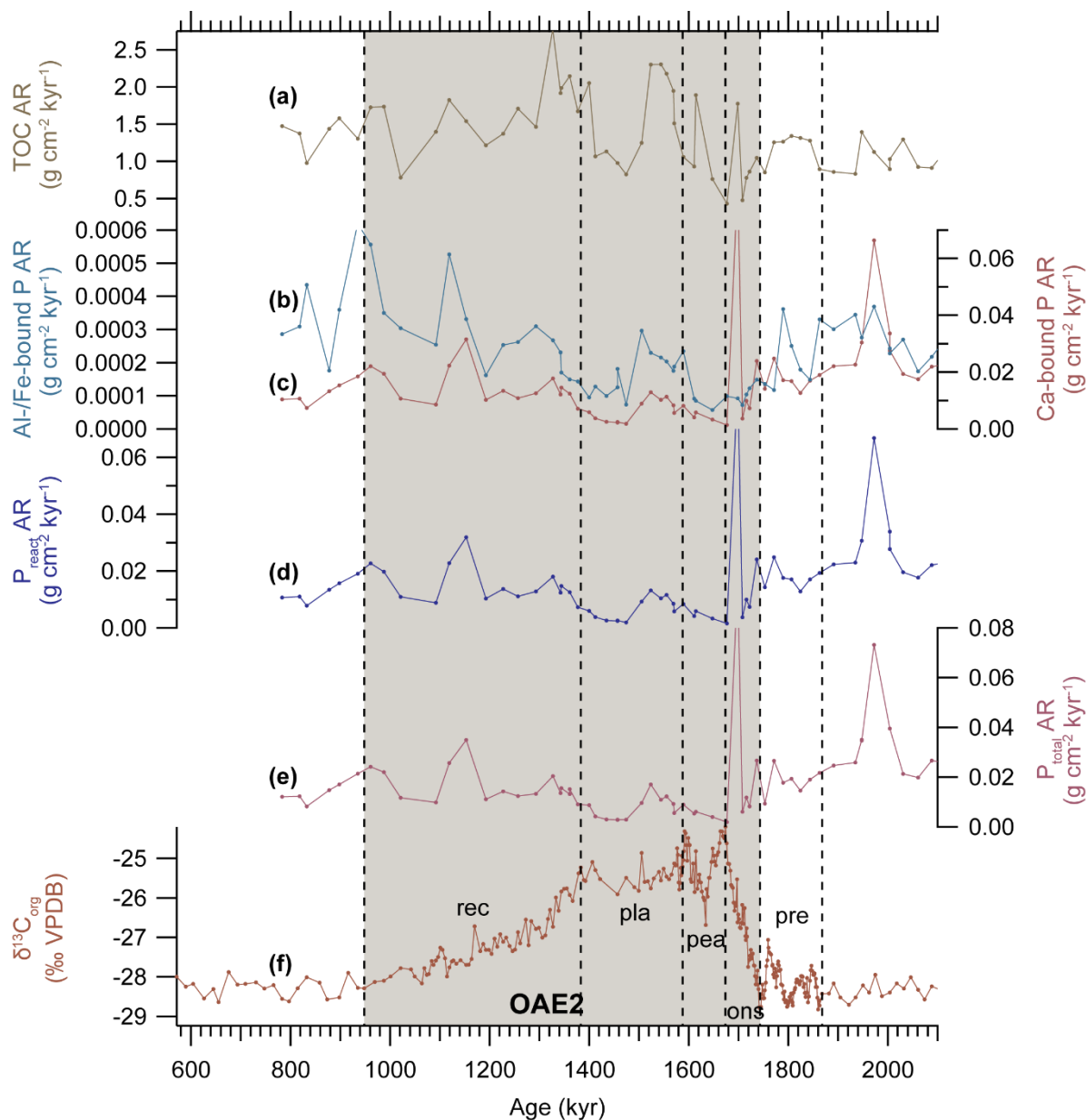
1040

Fig. 8. Phosphorus accumulation rates across OAE2 in Core SN°4 (age model based on Meyers et al. 2012). **(a)** Accumulation rate of
organic carbon (TOC AR). **(b)** accumulation rate of aluminium and iron bound phosphorus (Al-/Fe-bound P AR). **(c)** accumulation rate of
calcium bound phosphorus (Ca-bound P AR). **(d)** accumulation rate of reactive phosphorus calculated as the sum of Al-/Fe- and Ca-bound
P (P_{react} AR). **(e)** accumulation rate of total phosphorus (P_{total} AR). **(f)** $\delta^{13}C_{org}$. Stable Isotope data, carbon content and organic carbon
concentrations from Kuhnt et al. (2017) and Beil et al. (2018). The different phases of OAE2 are indicated as vertical black dashed lines.

1045

1050